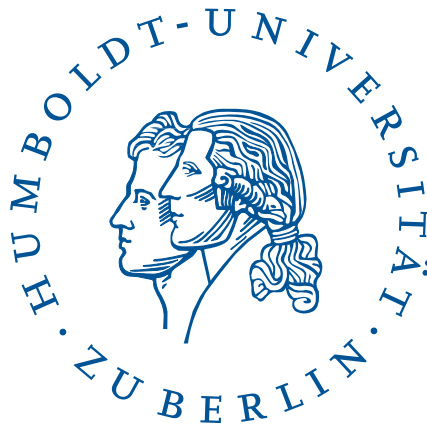


***Ab-initio* study of the thermoelectric clathrate**

**$\text{Ba}_8\text{Ni}_x\text{Ge}_{y-x}$ ($x = 0 - 6$, $y = 44 - 46$):
Ground states and electronic properties**

MASTERARBEIT

**zur Erlangung des akademischen Grades
Master of Science
(M. Sc.)
im Fach Physik**



**eingereicht an der
Mathematisch-Naturwissenschaftlichen Fakultät
Institut für Physik
Humboldt-Universität zu Berlin**

von

Herrn Martin Kuban

geboren am 12.02.1992 in Rüdersdorf bei Berlin

Gutachter:

1. *Prof. Dr. Claudia Draxl*
2. *Prof. Dr. Igor Sokolov*

In this work, a density-functional theory *ab-initio* study of the type-I clathrate compound $\text{Ba}_8\text{Ni}_x\text{Ge}_{46-x-y}\square_y$ ($x \in [0, 6], y \in [0, 2]$) is performed. The clathrate alloys form a "host" cage-like structure (Ge atoms) which can contain "guest" species (Ba atoms). It has been shown that this structure leads to a glassy thermal conductivity, i.e. they behave as thermal isolators. Moreover, the electronic properties can be tailored by substituting the atoms of the host lattice by non-isoelectronic species (Ni and vacancies). These characteristics make clathrate materials promising candidates for thermoelectric applications. In this study, an *ab-initio* description of the structural and electronic properties of $\text{Ba}_8\text{Ni}_x\text{Ge}_{46-x-y}\square_y$ is obtained. To achieve this goal, an essential step is to find the ground-state (GS) configurations, i.e. the specific arrangements of Ni atoms and vacancies in the host lattice which are lowest in energy. It is shown that the number of possible configurations presents a combinatorial explosion, hindering the realization of *ab-initio* calculations for every structure in the search for the GSs. To tackle this issue, extensive explorations of the configurational space are performed by means of a novel iterative cluster expansion (CE) approach. This CE makes use of a relatively small number of *ab-initio* calculations for well-selected structures to extract the relevant interactions. Once these are obtained, computationally inexpensive evaluations of the total energy can be performed. In this way, the GSs are found in a fully unbiased way, without any presumption regarding previous knowledge for other clathrate compounds. A good agreement with available experimental data concerning the lattice parameters of the thermodynamically stable structures at different compositions is obtained. For charge-balanced compositions (i.e. those with a closed-shell valence configuration in the host lattice) a pseudo band-gap at the Fermi level is revealed, while for charge-unbalanced compositions either *p*- or *n*-type behavior is found. These findings are fully compatible with reported measurements uncovering semiconducting behavior for charge-balanced compositions and a *n*- to *p*-type transition for unbalanced ones.

Contents

1	Introduction	1
2	Clathrates	4
2.1	Clathrate structure	4
2.2	The $\text{Ba}_8\text{Ni}_x\text{Ge}_{46-x-y}\square_y$ clathrate	5
3	Cluster-expansion method	7
3.1	Fundamentals of the cluster expansion	7
3.2	Inversion of the CE	9
3.3	Validation and cluster selection	11
3.4	Cluster-expansion package - CELL	12
4	Ab-initio calculations	14
4.1	Density-functional theory	14
4.2	Linearized augmented plane-waves	15
4.3	Methods for structure optimization	18
4.4	Computational parameters	20
5	Results	22
5.1	Ground-state searches	22
5.1.1	CE based on unrelaxed structures	25
5.1.2	CE based on relaxed structures	27
5.1.3	Effect of relaxation	28
5.2	Properties of the ground-state configurations	29
5.2.1	Thermodynamic stability	29
5.2.2	Structural properties	31
5.2.3	Electronic structure	33
6	Conclusions	37
A	Convergence tests	I
A.1	Convergence of energy differences for different configurations	I
A.2	Convergence of volume relaxations	I
A.3	Convergence of atom relaxation	IV
	Bibliography	VI
	List of Figures	VII
	List of Tables	IX

The thermoelectric effect allows for the conversion of heat into electricity. Using this effect, the waste heat generated e.g. in power plants, cars, etc. could in principle be recovered. However, their use on a large scale is hampered by a rather poor efficiency of the currently available materials. Thus, the search for new materials with high thermoelectric efficiency is crucial for the future of thermoelectric energy conversion.

The thermoelectric effect was discovered by Seebeck in 1821 [1]. It is sketched in Fig. 1.1. When exposed to a temperature gradient, charge carriers (electrons and holes) in a solid diffuse from the hot side to the cold side. This leads to a potential difference ΔV between the two sides of the material. The proportionality factor between ΔV and the temperature difference ΔT is the Seebeck coefficient

$$S = \frac{\Delta T}{\Delta V}. \quad (1.1)$$

The efficiency of a thermoelectric material is related to the dimensionless figure of merit ZT :

$$ZT = \frac{\sigma S^2 T}{\kappa}, \quad (1.2)$$

where σ is the electrical conductivity, T is the temperature, and κ is the thermal conductivity. In order to maximize ZT , one should increase the power factor σS^2 and minimize κ .

The thermal conductivity is the sum of two contributions, one of them due to lattice vibrations (phonons) κ_l and the other due to heat transport by charge carriers κ_e :

$$\kappa = \kappa_l + \kappa_e. \quad (1.3)$$

The electric conductivity and the electrical part of the thermal conductivity are approximately related to each other by the Wiedemann-Franz law:

$$\kappa_e = LT\sigma, \quad (1.4)$$

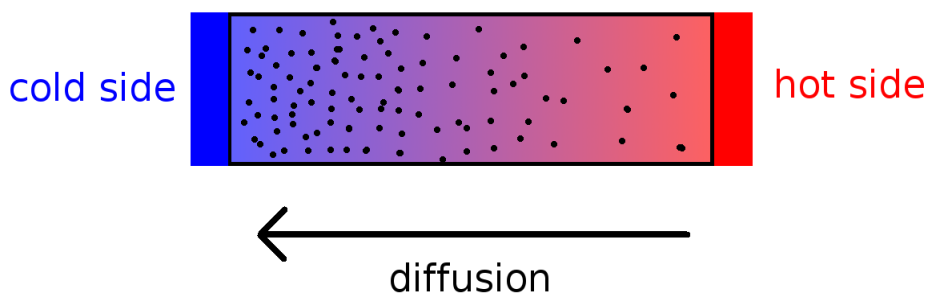


Figure 1.1.: Diffusion of charge carriers in a solid due to the presence of a temperature gradient.

with the proportionality factor L , being the so called Lorenz number. Therefore, one can not easily increase one property without increasing the other one as well. Thus, the maximization of ZT is difficult. A possible solution to this problem is offered by doped small band-gap semiconductors, for which κ_l is much larger than κ_e . This allows to decouple the electronic and vibrational degrees of freedom and leads to the concept of a 'phonon-glass electron-crystal' (PGEC). In this concept, the materials properties could be modified in such a way, that the thermal conductivity is minimized to obtain a 'glassy' behavior, but the electric conductivity is still high like in a crystal. Recent experiments show [1], that complex structures (such as clathrates, see Chap. 2) allow for a significant lowering of the lattice thermal conductivity, while keeping good electronic properties.

Figure 1.2 shows a scheme of a thermoelectric generator, consisting of two materials, one with p -type conductivity and the other with n -type conductivity. They form a conductive junction at one end, which is placed at the heat source. Both positive (holes, in the p -type material) and negative (electrons, in the n -type material) charge carriers diffuse to the cold side of the device. This introduces a charge accumulation of electrons at the cold side of the n -type material and holes at the cold side of the p -type material. The resulting potential difference is:

$$\Delta V = (S_1 - S_2)\Delta T, \quad (1.5)$$

where S_1 and S_2 are the Seebeck coefficients of material 1 and 2, respectively. To maximize this potential difference, usually two materials with different signs for the Seebeck coefficient are used, as provided by the materials with n - and p -type conductivity in Fig. 1.2.

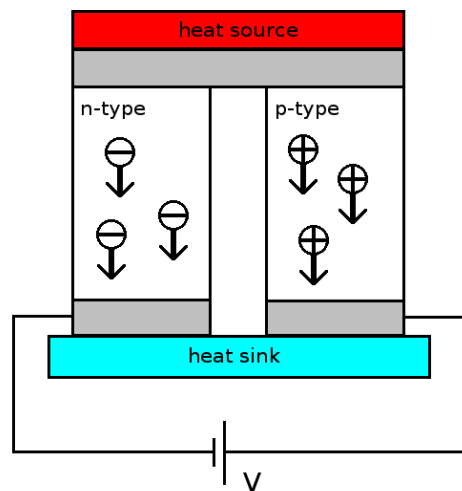


Figure 1.2.: Scheme of a thermoelectric generator. Charge carriers (electrons (-) and holes (+)) diffuse from the heat source to the heat sink (see Fig. 1.1), resulting in a voltage V .

To achieve increased efficiency and mechanical stability it is beneficial to use the same base materials for the construction of the junction. However, this requires the simultaneous achievement of good thermoelectric properties upon p - and n -type doping.

In this thesis, I study the intermetallic clathrate compound $\text{Ba}_8\text{Ni}_x\text{Ge}_{46-x-y}\square_y$ (the symbol \square denotes a vacancy) from a theoretical point of view. Germanium-based

clathrates have been the subject of several recent experimental and theoretical studies [2, 3, 4, 5, 6, 7]. They exhibit a significantly lower thermal conductivity compared to bulk Ge (phonon glass), while preserving reasonable electric conductivity (electron crystal). Furthermore, they have been synthesized in different compositions, which results in either *n*- or *p*-type conductivity. Thus, they fulfill the requirements for a PGEC, what makes them promising candidates for thermoelectric applications and an interesting compound to study.

I perform an in-depth *ab-initio* theoretical study of the structural and electronic properties of the $\text{Ba}_8\text{Ge}_{46}$ clathrate upon doping with Nickel atoms and in presence of vacancies. To achieve this, $\text{Ba}_8\text{Ni}_x\text{Ge}_{46-x-y}\square_y$ clathrates are simulated with *ab-initio* density-functional theory calculations, using the full-potential all-electron density-functional package **exciting**. The investigated composition range is $x = 0 - 6$, $y = 0 - 2$. One main goal is to find the ground-state configurations, i.e. the specific arrangements of Ni atoms and vacancies in the host lattice which are lowest in energy, out of all possible configurations. This is a very demanding task due to the large size of the configurational space: For each composition (i.e. one specific choice of x and y), there is a huge number of configurations. The *ab-initio* calculation of all possible configurations is practically impossible due to the computational cost involved. For this reason we apply an iterative cluster expansion approach, which allows for an extremely fast and accurate determination of the energy of any arbitrary configuration.

In this thesis, at first the studied clathrate compounds and the cluster-expansion approach are introduced. In the following chapter, details on the performed *ab-initio* calculations and methods for the reduction of the computational cost are presented. Finally, the search for ground-state structures with the cluster expansion and properties of the ground-state configurations of the clathrates are presented and discussed.

The clathrate structure was discovered in 1811 by Davy [8]. The crystal structure was identified using x-ray diffraction in 1935 by Pauling [9]. It was found to be formed at the ocean floor, when water can assemble under pressure into a cage-like structure, in which gases can be trapped. Clathrates can be formed by group IV elements [2]. In 1998 Nolas *et. al.* found out, that the concept of the PGEC can be applied to Ge-based clathrates and stated them to be promising candidates for thermoelectric applications [2], because they provide a very low (compared to bulk Ge) thermal conductivity, while preserving good electric conductivity. Thus, they fulfill the requirements for a true PGEC.

2.1. Clathrate structure

Figure 2.1 shows the structure of a type-I clathrate. It consists of 46 host atoms in the unit cell, occupying the $24k$, $16i$, and $6c$ Wyckoff sites of space group $Pm\bar{3}n$ (Nr. 223). These atoms form two dodecahedral and six tetrakaidecahedral cages. The centers of the cages are at the $2a$ and $6d$ Wyckoff sites, where up to eight guest atoms can be located [10]. Thus, the unit cell consists of a total number of 54 atoms. The guest atoms can be alkaline and alkaline earth atoms, which, due to the weak coupling to the host lattice, vibrate at low frequencies, acting as rattlers to scatter phonons and thus lower the lattice part of the thermal conductivity κ_l [11]. The guest atoms can donate their outer valence electrons, altering in this way the number of free charges in the host lattice. The atoms of the host lattice can be replaced by different substitutional atoms to tune the electrical properties of the crystal (see Section 2.2).

In this structure, host atoms are covalently bonded, while guest atoms form ionic bonds with the host. As can be seen in Fig. 2.1, the host atoms are tetrahedrally coordinated. A $24k$ -site has two $16i$, one $24k$, and one $6c$ neighbors. A $16i$ -site has three $24k$ -sites and one $16i$ -site as neighbors. Finally, the neighbors of a $6c$ -site are four $24k$ -sites. In total, there are four possible types of nearest neighbors: $24k$ - $24k$,

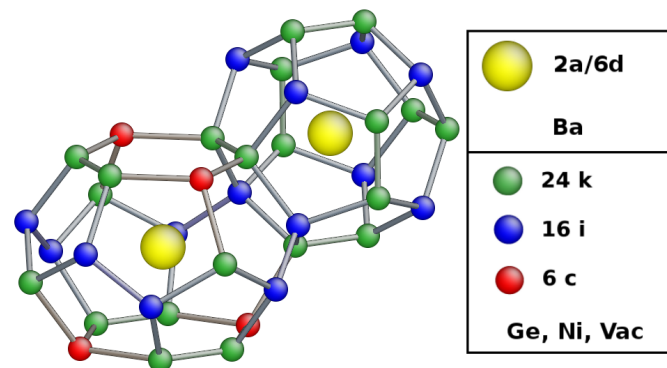


Figure 2.1.: Type-I clathrate structure. Wyckoff positions are indicated.

24k-16i, 24k-6c, and 16i-16i.

The electronic properties of the clathrate compound $\text{Ba}_8\text{Ni}_x\text{Ge}_{46-x-y}\square_y$, can be tailored either by substituting Ge atoms with Ni atoms or by introducing vacancies. Since the number of Ba atoms in the unit cell was found to remain constant for a wide composition range [3], only the configurational space of the host lattice is considered in this work. Thus, the present system can be treated as a quasi-ternary, formed from Ge, Ni and vacancies.

For a structure with 46 atoms in the host lattice, the number of possible configurations is huge. For a given composition, this number can be estimated by the following inequality:

$$\frac{1}{N_{sym}} \frac{N!}{x!y!(N-x-y)!} \leq n \leq \frac{N!}{x!y!(N-x-y)!} \quad (2.1)$$

with N the number of lattice points, x the number of substitutional Ni atoms, y the number of vacancies, and N_{sym} the maximum possible number of symmetrically equivalent configurations, which corresponds to the maximum Wyckoff multiplicity (i.e. 24 for the 24k-site). Figure 2.2 shows the combinatorial explosion of the number of configurations for a ternary compound with $N = 46$ and $N_{sym} = 24$. As can be seen, this number increases exponentially with the number of Ni atoms and vacancies. Already for six Ni atoms and two vacancies, it can be as large as 10^{10} .

2.2. The $\text{Ba}_8\text{Ni}_x\text{Ge}_{46-x-y}\square_y$ clathrate

$\text{Ba}_8\text{Ni}_x\text{Ge}_{46-x-y}\square_y$ can be synthesized by melting stichometric amounts of Ge, Ni, and Ba atoms and steel-quenching the melt [3]. Possible by-products of the synthesis are $\alpha - \text{Ge}$ and $\text{Ba}_6\text{Ge}_{25}$. For Ni concentrations of $x \geq 4.2$, samples showed increasing amounts of NiGe and/or BaGe₂ [3].

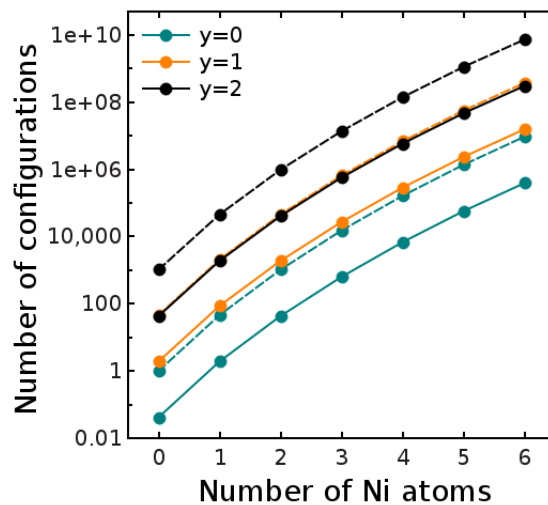


Figure 2.2.: Estimate of the number of configurations for a ternary compound with 46 atoms and a maximum of 24 symmetrically equivalent positions.

For Ni contents lower than $x = 1$, a $2a \times 2a \times 2a$ supercell was found [3], which changes to a primitive unit cell for $x \geq 1$. In the range $0.2 \leq x \leq 1.0$, Ni atoms can fill up a vacancy or substitute Ge atoms. Between $1.0 < x \leq 4.2$, Ni atoms progressively fill up vacancies. Above $x = 4.2$, no stable clathrates are found[3]. Higher Ni concentrations, without the presence of vacancies, are reported to be stable in [5, 6, 7]. For all these concentrations the measured lattice parameter remains approximately constant around the value $\sim 10.67 \text{ \AA}$.

Charge balance

In the empty Ge_{46} clathrate (i.e. the host structure without guest atoms), every Ge atom is covalently bonded to four neighboring Ge atoms, forming a closed-shell structure. Thus, it is expected to be a semiconductor. The addition of Ba atoms in the cavities leads to a metallic state. This is expected from the ionic guest-host interaction, implying that the 16 2s valence electrons of the Ba guests occupy the conductance band. In order to compensate these free charges and reach a semiconducting state, Ge atoms are substituted by Ni atoms or Ge vacancies need to be created. A substitutional Ni atom acquires the same valence configuration as Ge by borrowing four electrons from the host structure. The four Ge atoms surrounding a vacancy absorb four electrons from the host to fill the dangling bonds. Thus, both Ni substitutions and vacancies absorb 4 electrons each. Therefore, charge compensation is expected when the total number of Ni substitutions plus vacancies is exactly 4.

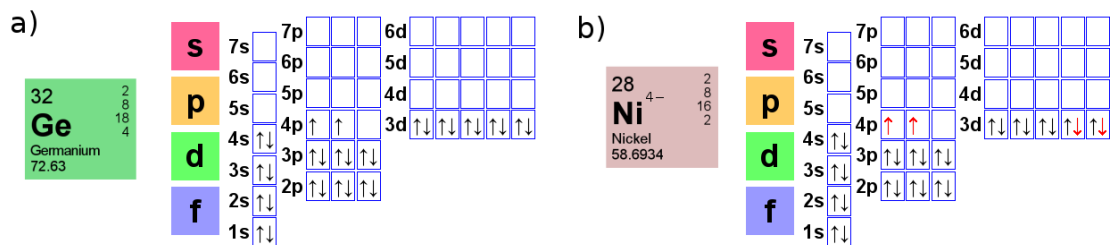


Figure 2.3.: Electronic configuration of Ge (a) and Ni (b) atoms in the host structure. Nickel atoms need four electrons (red arrows) to acquire the same valence configuration as Ge. Source: [12]

As shown in the previous section, the configurational space increases exponentially with the number of substituents. A main goal of this thesis is to find the lowest-energy configurations, i.e. the ground states, from the huge number of possible configurations. To achieve this, the energy of every configuration must be calculated. Calculating *ab-initio* data for billions of configurations is impossible, even with the fastest supercomputers on earth. For these reason, an alternative approach for the calculation of the total energy is required. The cluster expansion (CE) method allows to build a mapping between configurations and any configurational-dependent material property. The numerical evaluation of this mapping is orders of magnitudes faster than performing *ab-initio* calculations, while offering similar accuracy.

This chapter gives an introduction to the theoretical background of the CE method and its application.

3.1. Fundamentals of the cluster expansion

The cluster-expansion method is used to expand any property P that is a function of the configuration in terms of clusters. A cluster α is a set of lattice sites $\{p, p' .. p''\}$:

$$\alpha = \{p, p' .. p''\}. \quad (3.1)$$

Clusters can be characterized by their size (i.e. the largest distance between any two sites of a cluster) and the number of lattice sites they contain.

For a system consisting of M different species, any arbitrary configuration in a set of n lattice sites can be expressed by the occupation vector $\vec{\sigma}$, where each component σ_i , $i \in [1, n]$, refers to the occupation of a specific lattice site. The components σ_i can take integer values from 0 to $M - 1$, depending on what species occupy site i .

The aim is to build a linear model $P(\vec{\sigma}) = \sum_{\alpha} f_{\alpha} \Phi_{\alpha}(\vec{\sigma})$, in terms of a set of cluster basis functions $\Phi_{\alpha}(\vec{\sigma})$. To this end it is necessary to define the scalar product between two arbitrary discrete scalar functions of the occupation vectors, $f(\vec{\sigma})$ and $g(\vec{\sigma})$ [13]:

$$\langle f, g \rangle = \rho_n^0 \mathbf{Tr}^{(n)} f \cdot g \quad (3.2)$$

with the trace operator $\mathbf{Tr}^{(n)}$:

$$\mathbf{Tr}^{(n)} = \sum_{\sigma_1} \sum_{\sigma_2} \dots \sum_{\sigma_n} \quad (3.3)$$

and the normalization constant:

$$\rho_n^0 = M^{-n}. \quad (3.4)$$

The scalar product (3.2) can be used to define single-site orthonormal basis functions $\Theta_\kappa(\sigma)$ in the configurational space:

$$\langle \Theta_\kappa(\sigma), \Theta_{\kappa'}(\sigma) \rangle = \delta_{\kappa, \kappa'} \quad (3.5)$$

The choice of basis functions is arbitrary, with the only requirement of fulfilling Eq. (3.5). A common choice for constructing an orthogonal basis is the use of trigonometric functions [14]:

$$\Theta_\kappa(\sigma) = \begin{cases} 1 & \text{if } \kappa \text{ is } 0 \\ -\cos(2\pi \lceil \frac{\kappa}{2} \rceil \frac{\sigma}{M}) & \text{if } \kappa > 0 \text{ and odd} \\ -\sin(2\pi \lceil \frac{\kappa}{2} \rceil \frac{\sigma}{M}) & \text{if } \kappa > 0 \text{ and even} \end{cases} \quad (3.6)$$

where both κ and σ are integer numbers between 0 and $M - 1$, and $\lceil \dots \rceil$ denotes the 'round up' operation [14]. For a ternary compound ($M = 3$), these basis functions are:

$$\begin{aligned} \Theta_0(\sigma) &= 1 \\ \Theta_1(\sigma) &= -\cos\left(2\pi \frac{\sigma}{3}\right) \\ \Theta_2(\sigma) &= -\sin\left(2\pi \frac{\sigma}{3}\right) \end{aligned} \quad (3.7)$$

These functions are depicted in Fig. 3.1 and were used to define the CE for the ternary compounds in this work.

The basis functions (3.6) can be used to construct an orthonormal basis set of multi-site cluster functions $\Phi_{\alpha s}(\vec{\sigma})$ with respect to the scalar product (3.2) in the

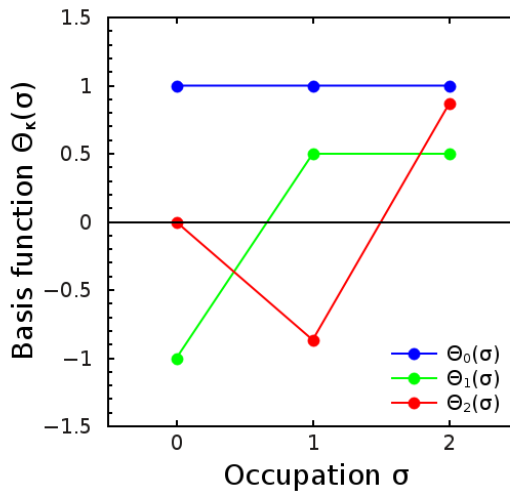


Figure 3.1.: Basis functions as defined in Eq. (3.6). These functions are defined in a discrete space, lines in the plot are guides to the eye.

following way:

$$\Phi_{\alpha s}(\sigma_p, \sigma_{p'}, \dots, \sigma_{p''}) = \Theta_{\kappa}(\sigma_p), \Theta_{\kappa'}(\sigma_{p'}), \dots, \Theta_{\kappa''}(\sigma_{p''}), \quad (3.8)$$

with $s = \{\kappa, \kappa' \dots \kappa''\}$ a set of indices containing the choice of the basis functions for each lattice site. Since they are orthonormal, they fulfill:

$$\langle \Phi_{\alpha s} \Phi_{\alpha' s'} \rangle = \delta_{\alpha\alpha'} \delta_{ss'}. \quad (3.9)$$

The cluster function for the empty cluster is by definition the unity [13]:

$$\Phi_{\alpha \equiv \{\emptyset\}} = 1. \quad (3.10)$$

With this basis, any function of the configuration can be expressed as a sum over cluster functions [13]:

$$f(\vec{\sigma}) = \sum_{\alpha} \sum_s f_{\alpha s} \Phi_{\alpha s}(\vec{\sigma}), \quad (3.11)$$

with the expansion coefficients

$$f_{\alpha s} = \langle \Phi_{\alpha s}, f \rangle. \quad (3.12)$$

This does not take into account any symmetry. For periodic lattices it can be shown [15] that the expansion coefficients $f_{\alpha s}$ adopt the space-group symmetry of the underlying lattice and therefore are independent of translations and rotations. With this knowledge, expression (3.11) can be rewritten as

$$f(\vec{\sigma}) = \sum_{\alpha} \sum_s m_{\alpha s} \tilde{J}_{\alpha s} X_{\alpha s}(\vec{\sigma}) \quad (3.13)$$

where $\tilde{J}_{\alpha s}$ are the effective cluster interactions (ECIs) and $X_{\alpha s}$ are the cluster correlation functions defined by:

$$X_{\alpha s}(\vec{\sigma}) = \frac{1}{m_{\alpha s}} \sum_{\beta \equiv \alpha} \Phi_{\beta s}(\vec{\sigma}), \quad (3.14)$$

where β are all $m_{\alpha s}$ clusters, that are symmetrically equivalent to cluster α .

3.2. Inversion of the CE

In this section, it is explained how to find the ECIs that give the best fit to a set of *ab-initio* calculations. Since the previously defined basis is infinite, it must be cut off in practical applications of the method. The derivations below assume a finite basis set of N_{clus} cluster functions. In Sec. 3.3 a way to obtain the optimal basis set will be explained.

A usual application of the cluster-expansion method is the fitting of a property

$P(\vec{\sigma})$ to a set of *ab-initio* data [15]. As a result of the fitting process the ECIs $\vec{J}_{\alpha s}$ are obtained and can be used to make predictions for unknown structures.

For a set of *ab-initio* calculations, Eq. (3.13) can be recast in matrix form:

$$\vec{P} = \mathbf{X}\vec{J}. \quad (3.15)$$

Here the vector \vec{P} has the values $(P(\vec{\sigma}_1), P(\vec{\sigma}_2), \dots, P(\vec{\sigma}_{N_c}))$, where the $P(\vec{\sigma}_c)$ is the calculated property for structure $\vec{\sigma}_c$, and N_c is the total number of *ab-initio* calculations. \mathbf{X} is a $N_c \times N_{clus}$ -dimensional matrix with elements $X_{\alpha s}(\vec{\sigma}_c)$. The matrix \mathbf{X} contains one row for every configuration c and one column for every cluster αs . A row of \mathbf{X} can be considered as a row vector and is denoted below as $\vec{X}(\vec{\sigma})$. The components of the vector \vec{J} are $J_{\alpha s} = m_{\alpha s} \vec{J}_{\alpha s}$.

The ECIs can be found by minimizing an objective function, as for instance the mean square error (MSE) of the predictions $\mathbf{X}\vec{J}$:

$$C(\vec{J}) = \frac{1}{N_c} \sum_c^{N_c} [P(\vec{\sigma}_c) - \vec{X}(\vec{\sigma}_c)\vec{J}]^2, \quad (3.16)$$

with N_c the number of structures in the training set and c denoting a configuration from the training set. The minimization is achieved by solving the equation:

$$\nabla_{\vec{J}} C(\vec{J}) = 0, \quad (3.17)$$

with the result

$$\vec{J} = (\mathbf{X}^T \mathbf{X})^{-1} \mathbf{X}^T \vec{P}. \quad (3.18)$$

When the number of clusters is larger than the number of structures, the matrix $\mathbf{X}^T \mathbf{X}$ has linearly dependent rows and cannot be inverted. This problem can be solved by adding a regularization term to Eq. (3.16):

$$C(\vec{J}) = \frac{1}{N_c} \sum_c^{N_c} [P(\vec{\sigma}_c) - \vec{X}(\vec{\sigma}_c)\vec{J}]^2 + \gamma \sum_{\alpha s}^{N_{clus}} J_{\alpha s}^2, \quad (3.19)$$

where the penalization factor γ is found by a validation procedure as will be explained in Sec. 3.3. This special choice of the regularization term is called ℓ_2 -norm. With this kind of regularization the components of \vec{J} will decrease, when γ increases.

By applying (3.17) to Eq. (3.19), the solution is:

$$\vec{J} = (\mathbf{X}^T \mathbf{X} + N_c \gamma I)^{-1} \mathbf{X}^T \vec{P}, \quad (3.20)$$

where I denotes the identity matrix. When fitting the ECIs to *ab-initio* data, the actual set of clusters is left as a free parameter. A proper selection of this set is crucial to get accurate predictions. This will be explained in the next section.

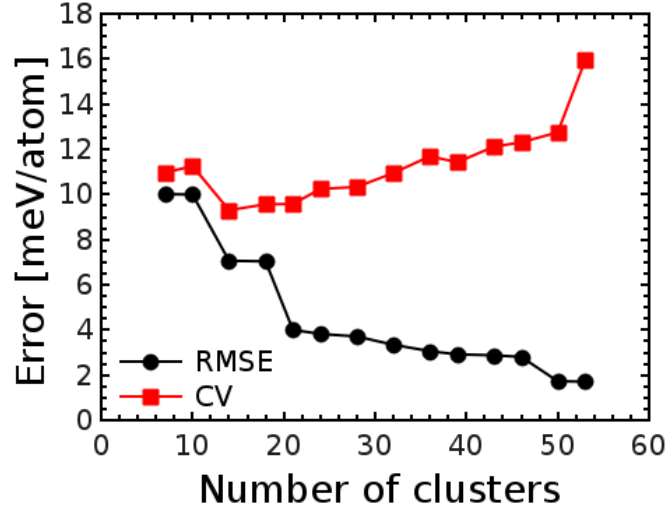


Figure 3.2.: Root mean square error (RMSE) and cross validation score (CV) as a function of the number of selected clusters.

3.3. Validation and cluster selection

To minimize the MSE of the fit, the number of clusters can be chosen arbitrarily high, the resulting MSE will decrease with increasing number of degrees of freedom for the fitting process. However, by choosing a too high number of clusters for the model, overfitting [16] occurs and predictions get worse. To overcome this issue, the cross-validation score (CV) is used. In this approach, a structure $\vec{\sigma}_c$ is removed from the training set and not used for fitting the effective cluster interactions $J_{\alpha S}$. Thus, the error of the prediction for the removed structure $\vec{\sigma}_c$ is a measure of the predictive power of the model. The leave-one-out-cross-validation (LOO-CV) is defined as:

$$CV = \sqrt{\frac{1}{N_c} \sum_c^{N_c} [\vec{P}(\vec{\sigma}_c) - \mathbf{X}_{(\sigma_c)} \vec{J}_{(\sigma_c)}]^2}, \quad (3.21)$$

where (σ_c) denotes the configuration σ_c , that is not used for calculating the effective cluster interactions. A low cross-validation score can be interpreted as high predictive power.

The cluster selection is based on the minimization of the CV score. This can be achieved in several ways. Below, two of them are explained.

One option is first forming several sets of clusters based on an educated guess. Clusters with few points and a small radius are expected to have a bigger contribution to the total energy than larger clusters. Thus, cluster sets are formed containing clusters of increasing number of points n and the radii r_{clus} . For every set of clusters, the CV and the root MSE (RMSE) are calculated. Typically, the RMSE decreases monotonically for increasing cluster set size, whereas the CV reaches a minimum and then may increase again, due to overfitting. An example of this is shown in Fig. 3.2, which presents this procedure for one of the clathrate data sets of this work. For this example, the set with the minimal CV, consisting

of 14 clusters, is chosen. The advantage of this technique is its simplicity and clearness. A disadvantage is, that it is based upon the educated guess and not on an extensive search of all possible combinations of clusters. However, for the studied systems, it led to accurate enough predictions and was the method selected for this work.

Another option is the use of compressed sensing. Here, a penalization term $\gamma \sum_{\alpha s}^{N_{clus}} |J_{\alpha s}|$ (i.e. a ℓ_1 -norm) is added to Eq. (3.16). This type of penalization favors sparsity by minimizing the number of non-zero ECIs [17]. Its application to the clathrates in this work did not give better results than the use of the method explained above.

3.4. Cluster-expansion package - CELL

CELL (Cluster expansion for large parent cells) [18] is a Python package that makes use of an iterative cluster expansion to sample the configurational space of structures with large unit cells. Conventional codes for cluster expansion usually rely on full enumerations of all possible configurations of substituents. This technique is not suitable for clathrates because of the large size of their unit cell (54 atoms), which leads to a combinatorial explosion of the number of configurations. To avoid this problem, **CELL** combines the cluster-expansion method with efficient samplings of the configurational space. The workflow of **CELL** is pictured in Fig. 3.3.

The search for the configurational ground state is started with an initial set of random structures (structures with a random distribution of substitutional atoms). For this set of structures, *ab-initio* energies are calculated. A cluster expansion is performed to obtain the effective cluster interactions. With these, one can predict the energy of new structures. The configurational space is extensively sampled and *ab-initio* energies are calculated for the lowest-energy configurations found in this way. These data points are added to the initial data set and the cycle starts again with the calculation of the ECIs. This procedure is repeated until no new ground states are found and the cross-validation score for the cluster expansion is low enough to make accurate predictions.

For this work, I extended **CELL** to work with ternary compounds. To achieve

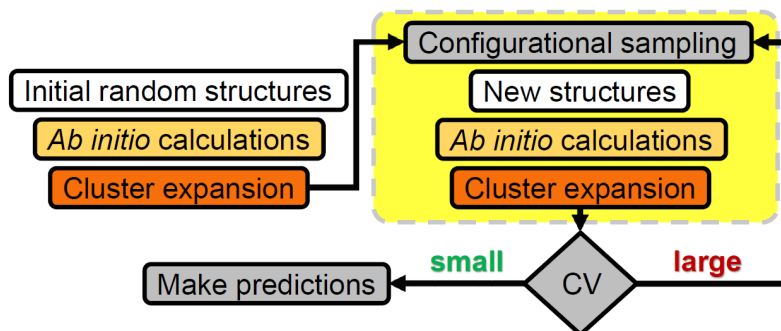


Figure 3.3.: Workflow of **CELL**. The steps are described in detail in the text. Figure from [18].

this, I updated (and in some cases developed) several routines for sampling the configurational space and creating new structures.

All *ab-initio* calculations in this work are done with the full-potential all-electron density functional theory (DFT) package **exciting** [19]. This package uses a basis set representation composed of linearized augmented plane-waves plus local orbitals. This basis allows for a high numerical precision.

This chapter briefly describes density-functional theory, and the Kohn-Sham (KS) equations are introduced. Afterwards, linearized augmented plane-waves, as implemented in **exciting**, for solving the KS equations are described. Also, several techniques, that are used to reduce the computational cost of volume optimizations of the studied compounds, are introduced. The last section of this chapter presents the computational parameters.

4.1. Density-functional theory

Density-functional theory is based on the Hohenberg-Kohn theorem [20] that states that the total energy E of a system of interacting electrons immersed in an external potential $v(\vec{r})$ can be written as a functional of the electron density $n(\vec{r})$ alone:

$$E[n] = F[n] + \int d\vec{r} v(\vec{r}) n(\vec{r}). \quad (4.1)$$

Here, $F[n]$ is a universal functional of the density, independent of the external potential $v(\vec{r})$. This approach has the advantage over wave-function based approaches, that it is only dependent on the electron density $n(\vec{r})$, which is a function of the three coordinates of the vector \vec{r} , instead of the N -particle many-body wave-function $\psi(\vec{r}_1, \vec{r}_2, \dots, \vec{r}_N)$ that depends on $3N$ coordinates. The exact expression for the universal functional $F[n]$ is unknown (except for a few simple cases) and thus must be approximated for practical applications.

In 1965, Kohn and Sham [21] have shown, that the many-particle problem of interacting electrons can be mapped to an effective system of non-interacting electrons, which has the same electron density as the real system. Thus, the Schrödinger equation of N interacting particles can be reduced to a single-particle Schrödinger equation:

$$\left[-\frac{1}{2} \nabla^2 + v_{\text{eff}}(\vec{r}) \right] \psi_i(\vec{r}) = \epsilon_i \psi_i(\vec{r}), \quad (4.2)$$

where $\psi_i(\vec{r})$ are single particle orbitals that are solutions of the KS equation, and ϵ_i is the eigenenergy corresponding to solution i . The effective potential v_{eff} can be split into a sum of three different terms:

$$v_{\text{eff}} = v_{\text{ext}} + v_{\text{H}} + v_{\text{XC}}, \quad (4.3)$$

where v_{ext} is an external single particle potential (e.g. interactions of electrons with ions in a solid), v_{H} is the Hartree potential, describing classical Coulomb interactions of electrons, and v_{XC} is the exchange-correlation potential, which relates to the difference between the exact Coulomb interaction and the Hartree approximation.

The exchange correlation potential v_{XC} is defined as the functional derivative of the exchange correlation energy E_{XC} with respect to the electron density $n(\vec{r})$:

$$v_{\text{XC}} = \frac{\delta E_{\text{XC}}}{\delta n(\vec{r})}. \quad (4.4)$$

The exact expression for E_{XC} in Eq. (4.4) is unknown and must be approximated. The simplest, but commonly used, approximation is the local density approximation (LDA), where the exchange-correlation energy E_{XC} is written as:

$$E_{\text{XC}}^{\text{LDA}}[n] = \int d\vec{r} n(\vec{r}) \varepsilon_{\text{XC}}(n), \quad (4.5)$$

where $\varepsilon_{\text{XC}}(n)$ is the exchange-correlation energy per particle of a homogeneous electron gas with density n . Several alternative approximations exist, as for instance the generalized-gradient approximation (GGA), which also takes the gradient of the electron density into account, and more accurate ones, like hybrid functionals, with an exact treatment of the exchange contribution. In reference [22], it is shown that the choice of v_{XC} between LDA and GGA does not affect the ground-state search for AlSi-based clathrates. Thus, only LDA was considered in this work.

The electron density is given by:

$$n(\vec{r}) = \sum_{i=1}^N |\psi_i(\vec{r})|^2. \quad (4.6)$$

Since the electron density is not known, the KS equation has to be solved self-consistently: An initial guess is used as input for $n(\vec{r})$. From this density, the effective potential is calculated using the Poisson equation for the Hartree potential and Eq. (4.4) for the exchange-correlation potential. The KS equation is solved and a new electron density is calculated using Eq. (4.6). With this new density, the procedure is repeated from the calculation of the effective potential, until $n(\vec{r})$ converges, i.e. it does not change significantly within new iterations.

4.2. Linearized augmented plane-waves

The code **exciting** uses the method of linearized augmented plane-waves (LAPW) for solving KS equations [19]. KS wavefunctions are constructed from a

superposition of augmented plane-waves:

$$\psi_{i\vec{k}}(\vec{r}) = \sum_{\vec{G}}^{|\vec{G}| < G_{\max}} C_{i\vec{G}}^{\vec{k}} \phi_{\vec{G}+\vec{k}}(\vec{r}), \quad (4.7)$$

where \vec{k} are vectors in the first Brillouin zone and \vec{G} are reciprocal lattice vectors. From these orbitals, the electron density is calculated with Eq. (4.6), where the sum runs over both the band-index i and vectors in the Brillouin zone \vec{k} . The space is separated into non-touching spheres, centered in the atoms (so called atomic spheres (AS)), and the interstitial, i.e. the space between the atomic spheres. For a numerical solution of the equations described in this section, the Brillouin zone must be discretized. In **exciting**, this discretization is controlled by the parameter `ngridk`, which specifies the number of k -points along every of the reciprocal primitive vectors. The scalar G_{\max} defines the maximal length of a reciprocal lattice vector that is used to cut off the basis of augmented plane-waves. This property is controlled by the **exciting** input parameter `rkgmax`, which is defined by: $rkgmax = R_{AS}^{\min} \cdot G_{\max}$, where R_{AS}^{\min} is the smallest atomic sphere radius. $C_{i\vec{G}}^{\vec{k}}$ are expansion coefficients and the augmented plane-waves $\phi_{\vec{G}+\vec{k}}(\vec{r})$ are defined as:

$$\phi_{\vec{G}+\vec{k}}(\vec{r}) = \begin{cases} \sum_{lm} A_{lm\alpha}^{\vec{G}+\vec{k}} u_{l\alpha}(r_{\alpha}) Y_{lm}(\hat{r}), & r_{\alpha} \leq R_{AS\alpha} \\ \frac{1}{\sqrt{\Omega}} e^{i(\vec{G}+\vec{k})\vec{r}}, & \vec{r} \in I. \end{cases} \quad (4.8)$$

In the AS regions ($r_{\alpha} \leq R_{AS}$), they are represented in a spherical basis and thus expanded in terms of spherical harmonics Y_{lm} and radial functions $u_{l\alpha}$ for each atom α . In the interstitial region ($\vec{r} \in I$), they are represented by plane-waves. $A_{lm\alpha}^{\vec{G}+\vec{k}}$ are coefficients used to make the augmented plane-waves continuous at the boundaries between the atomic sphere region and the interstitial. That is, every plane-wave in the interstitial is matched to a linear combination of radial functions in the atomic spheres in order to achieve continuity.

In order to find the radial functions $u_{l\alpha}$ of Eq. (4.2), the effective potential $v_{\text{eff}}(\vec{r})$ of Eq. (4.2) can be approximated in the AS regions by the spherical average $v_0(r)$, assuming spherical symmetry. Then, the radial part of Eq. (4.2) can be written as:

$$\left[-\frac{1}{2} \frac{d^2}{dr^2} + \frac{l(l+1)}{2r^2} + v_0(r) - \epsilon_{i\mathbf{k}} \right] (ru_{l\alpha}(r)) = 0 \quad (4.9)$$

The solution of this equation is dependent on the energy $\epsilon_{i\mathbf{k}}$, thus introduces a non-linearity. To overcome this issue, the $\epsilon_{i\mathbf{k}}$ are set to a fixed value $\epsilon_{l\alpha}$ for each l channel. This leads to a mismatch of this energy parameter with the actual eigenenergy $\epsilon_{i\mathbf{k}}$. The error introduced by this mismatch can be reduced by introducing the first derivative of the radial functions with respect to ϵ , $\dot{u}_{l\alpha}$, to the APW basis in the atomic sphere regions, forming the LAPW basis:

$$\phi_{\vec{G}+\vec{k}}(\vec{r}) = \sum_{lm} \left[A_{lm\alpha}^{\vec{G}+\vec{k}} u_{l\alpha}(r_{\alpha}; \epsilon_{l\alpha}) + B_{lm\alpha}^{\vec{G}+\vec{k}} \dot{u}_{l\alpha}(r_{\alpha}; \epsilon_{l\alpha}) \right] Y_{lm}(\hat{r}), \quad r_{\alpha} \leq R_{AS} \quad (4.10)$$

where $B_{lm\alpha}^{\vec{G}+\vec{k}}$ are new coefficients to achieve a smooth derivative of the augmented plane-waves at the boundaries of the AS regions. It has been found [19] that the matching of the derivative in the boundary has a strong effect on the shape of the radial functions inside the atomic sphere. In order to avoid this problem, the term proportional to \dot{u} in Eq. (4.10) is removed and so-called local orbitals are constructed. These orbitals are a linear combination of u and \dot{u} , and are explicitly zero outside the atomic spheres. The coefficients are determined from the constraints of normalization and the vanishing at the atomic sphere boundary. In this way, a better basis, which preserves the flexibility given by the term \dot{u} and does not require the matching of the second derivative, is obtained. This is the basis used in this work and is termed APW+lo.

4.3. Methods for structure optimization

The calculation of *ab-initio* energies with DFT requires the optimization (or relaxation) of the structural parameters, i.e. lattice constants and atomic positions. For clathrate structures, this is a demanding task because of the large size of the unit cell. The presence of vacancies additionally makes the relaxations more difficult. Thus, several techniques for reducing the computational cost of these structural optimizations are used. They are introduced in this section.

First, lattice constant values a are sampled through the Nelder-Mead (NM) algorithm together with fits to the Birch-Murnaghan (BM) equation of states [23], which provides a description of the total energy E of a solid in terms of its unit cell volume:

$$E(V) = E_0 + \frac{9}{16}B_0V_0 \left(\left[\left(\frac{V_0}{V} \right)^{\frac{2}{3}} - 1 \right]^3 B'_0 + \left[\left(\frac{V_0}{V} \right)^{\frac{2}{3}} - 1 \right]^2 \left[6 - 4 \left(\frac{V_0}{V} \right)^{\frac{2}{3}} \right] \right) \quad (4.11)$$

Here, E_0 is the energy of the relaxed crystal, V_0 is the volume of the relaxed crystal, V the volume of a strained crystal and B_0 and B'_0 are the bulk modulus and its first derivative with respect to the pressure, respectively.

Since the number of free parameters in Eq. 4.11 (E_0 , V_0 , B_0 and B'_0) is four, at least five calculations with different lattice constants are required.

From an initial value of a , the NM algorithm automatically samples values of a in its neighborhood and proposes new values of a for the calculation of the energy, thus approaching the minimum of the energy $E(a)$ as a function of a . After a preselected number of steps (typically seven steps), this algorithm is interrupted and a BM fit is performed. With the lattice constant obtained from the fit, another ground-state calculation is performed, enlarging the set of *ab-initio* calculations. The full data set is fitted again. The a resulting from this last fit is used to perform an atom relaxation. Subsequent volume and atom position relaxations are performed, until no further changes are obtained. Typically, two iterations are required.

The process of NM+BM lattice relaxation is shown in Fig. 4.1. Here, black dots represent energies for lattice constants that are obtained by the NM algorithm. The numbers represent the order of calculations. As can be seen, the sampled lattice constants approach the minimum in energy. The sampling gets denser in the surrounding of the minimum. The red dot indicates the lattice constant that is obtained from fitting the BM to the black dots. The red line is the fit of the BM to all points.

The self-consistency loop (SCL) in **exciting** is stopped when the absolute energy differences between the last three SCL iterations are below a certain threshold E_{thres} . In reference [22], it was noted that applying this criterium to all the values of a in the NM+BM method leads to a waste of computational resources, since the energy differences between structures with different a usually converge faster than the total energy. Thus, a considerable gain of computational effort was obtained by

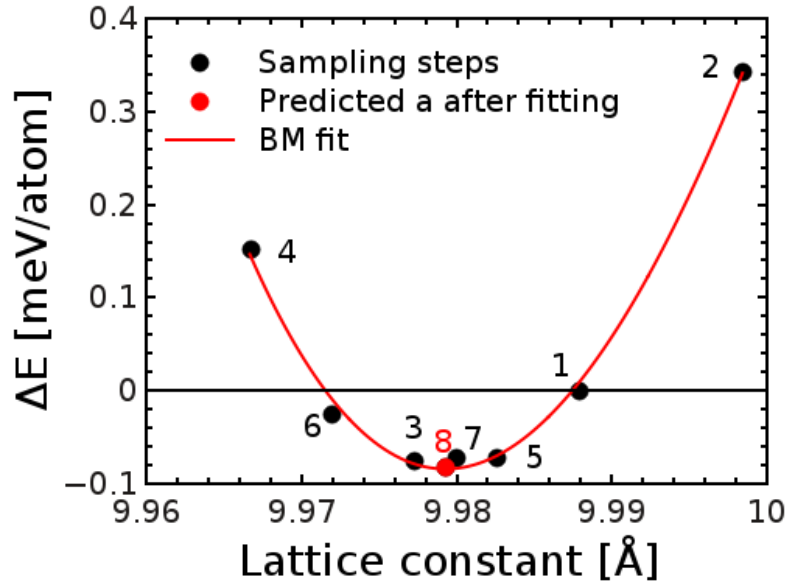


Figure 4.1.: Example of the NM+BM lattice relaxation. All energies are given as a difference to the first calculation of this set. Black dots represent *ab-initio* energies. The red dot indicates the lattice constant from the BM fit to the black dots. The red curve shows the final fit with the BM equation of states including the red dot. The index of the calculation is indicated by a number.

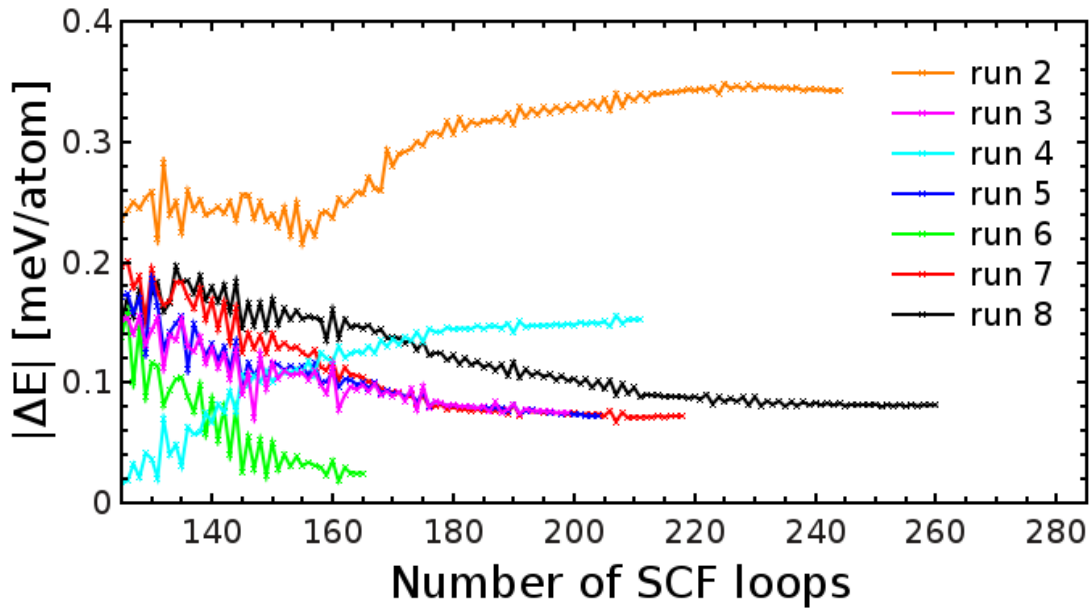


Figure 4.2.: Convergence of SCL iterations in energy differences $|\Delta E|$ to run 1.

first performing a calculation for an initial a (called here run 1) with a small E_{thres} . Then, the SCL loop for the other values of a is stopped whenever the absolute energy difference with respect to run 1 is below this threshold. This is shown in Fig. 4.2 for the same data as in Fig. 4.1. The ordinate shows the absolute energy differences of the SCL iterations with respect to run 1.

Besides generating data sets with fully optimized structures, also data sets with non-optimized structures were considered. In that case the lattice coordinates of the atoms were fixed to that of the relaxed pristine $\text{Ba}_8\text{Ge}_{46}$ clathrate, and the lattice constant was estimated from the application of Vegard's law. In this case, the lattice

constant is considered to be linearly dependent on the number of substituents. For this ternary compound, Vegard's law was applied by interpolating between the compounds $\text{Ba}_8\text{Ge}_{46}$, $\text{Ba}_8\text{Ni}_6\text{Ge}_{40}$ and $\text{Ba}_8\text{Ge}_{44}\square_2$:

$$a(x, y) = a_{(0,0)} + (a_{(6,0)} - a_{(0,0)})\frac{x}{6} + (a_{(0,2)} - a_{(0,0)})\frac{y}{2}, \quad (4.12)$$

where $a_{(x,y)}$ is the lattice constant of a relaxed structure with composition (x, y) .

4.4. Computational parameters

This section presents details about the parameters that are used for *ab-initio* calculations performed in this work. The convergence tests, leading to these parameters, are presented in App. A.

For the extensive sampling of the configurational space, it is crucial that the energy differences between structures with similar configurations are converged with the computational parameters of the simulation. To test this convergence, five configurations with different neighboring relations (i.e. different number of first, second, third nearest neighbors) of the substitutional Ni atoms, were created manually. Their energy was calculated for increasing `rgkmax` and `ngridk`.

Table 4.1 presents the results of this test. Here, the neighboring relationship between Ni atoms is represented by a tuple of three numbers: (No. of nearest neighbors, No. of second nearest neighbors, No. of third nearest neighbors). The calculated energies are presented in reference to configuration 4. The converged parameters, that led to these energies are `ngridk` = $2 \times 2 \times 2$ and `rgkmax` = 6.

From this table, the resolution in energy that is required to distinguish between

Index i	1	2	3	4	5
Neighbors	(1, 1, 0)	(0, 0, 2)	(0, 1, 1)	(0, 2, 0)	(0, 2, 0)
$\Delta E_{i,4}$ $\left[\frac{\text{meV}}{\text{atom}} \right]$	39.04	9.50	15.14	0	2.22

Table 4.1.: Comparison of energies differences $\Delta E_{i,4} = E_i - E_4$ of different configurations of the $\text{Ba}_8\text{Ni}_3\text{Ge}_{43}$ clathrate. The tuples indicate the neighboring relations of the Ni atoms: (No. of nearest neighbors, No. of second nearest neighbors, No. of third nearest neighbors).

two different configurations, can be estimated. For configurations with the same type of neighbors (configurations 4 and 5), a resolution in energy of $\Delta E = 2.22$ meV/atom is necessary. The energy difference that is introduced by the creation of a bond between two Ni atoms can be estimated by comparing structure 1 and 4. Here, the position of one Ni atom in configuration 1 is changed, such that in configuration 4 it is not a nearest, but a second nearest neighbor. The resulting energy difference is $\Delta E = 39.04$ meV/atom.

The following paragraph presents the parameters that led to converged results of lattice and atom relaxations. Lattice relaxations in this work were performed with $ngridk=2 \times 2 \times 2$ and $rgkmax=6$. Although the thus obtained lattice constants are not converged with this choice of $rgkmax$, it is shown in App. A.2 that the ordering of configurations is already converged. Therefore, these parameters can be used for the GS search. In order to obtain more realistic results for the lattice constant, $rgkmax=8$ is chosen for the calculation of the properties of the ground-state configurations.

Well converged forces for the structure optimization were achieved with the simulation parameters $rgkmax=6$ and $ngridk=2 \times 2 \times 2$.

For electronic structure calculations, $rgkmax=8$ and $ngridk=8 \times 8 \times 8$ are used.

Table 4.2 presents an overview of the converged computational parameters for different tasks in this work.

	Volume relaxation	Structure relaxation	GS-search	GS
$rgkmax$	6	6	6	8
$ngridk$	$2 \times 2 \times 2$			
ϵ_{force} [meV/Å]	/	257.11	/	/
E_{thres} [meV/atom]	$5.04 \cdot 10^{-6}$	$5.04 \cdot 10^{-3}$	$5.04 \cdot 10^{-3}$	$5.04 \cdot 10^{-3}$

Table 4.2.: Computational parameters leading to converged quantities.

Even with the techniques introduced in this section, the relaxation is still costly. A reasonable fit with the BM equation of state for the volume relaxation requires eight sampling steps. Each atom relaxation requires at least one ground-state calculation to determine the forces. After each update of the atomic positions, a new ground-state calculation is performed. A full atom relaxation can require up to 60 structure optimization steps. This high amount of ground-state calculations is needed because of the large distortions of the lattice due to the presence of vacancies.

This has been tested for an excited (i.e. non-GS) configuration with composition $(x, y) = (4, 1)$. The average change Δd in bond distances to the four atoms surrounding either a Ni atom or a vacancy are considered. For the first, $\Delta d_{Ni} = 0.10$ Å, and for the second $\Delta d_{\square} = 0.51$ Å. Thus, the presence of vacancies introduce large distortions in the structure.

This chapter is organized as follows: In Sec. 5.1 the GS searches for the whole composition range is presented. Next, the thermodynamical stability, and structural and electronic properties of the found GSs are presented in Sec. 5.2.

5.1. Ground-state searches

For the search of the configurational GSs, two approaches are used. In the first approach, the CE was performed on a structure set that makes use of Vegard's law for approximating the lattice constant, while the internal coordinates of the atoms are fixed to that of the pristine clathrate $\text{Ba}_8\text{Ge}_{46}$. In the second approach, fully optimized structure sets are used to perform the CE. In the following, "unrelaxed set" and "relaxed set" I call the set of structures generated by using the first approach and the set of structures generated by using the second approach, respectively.

The CE for both sets was performed for the energy of mixing, which is defined as:

$$E_{mix} = E - \left(E_0 + (E_1 - E_0) \frac{x}{x_{ref}} + (E_2 - E_0) \frac{y}{y_{ref}} \right), \quad (5.1)$$

where E is the total energy of a structure with x Ni atoms and y vacancies, E_0 is the energy of the pristine structure, E_1 is the energy of a structure with x_{ref} Ni atoms and no vacancies, and E_2 is the energy of a structure with y_{ref} vacancies and no Ni atoms.

As an example, the GS search for the unrelaxed set is explained in detail for $y = 2$ and $x = 0 - 6$. The GS search for the full unrelaxed and relaxed sets proceeded in an analogous fashion.

The ground-state search is performed following the workflow of **CELL** as shown in Sec. 3.4. The results of this procedure are presented in Fig. 5.1, illustrating the performance of the algorithm.

In panel a) of this figure, the set of random structures (represented by black dots) is used to find an initial CE model.¹ Using this model, the configurational space is extensively sampled. The energies of the sampled configurations are calculated with the CE and are represented by red crosses. The algorithm predicts one ground-state configuration per composition. These are represented by green squares. The *ab-initio* energies of these configurations are calculated. The results are shown as green dots in panel b). The predictions for $x \leq 3$ are moderately good, but for higher values the predicted energies differ considerably from the calculated values. The new data obtained in this second iteration is used to enlarge the training set,

¹For simplicity, only the data for $y = 2$ is presented. Here and in the subsequent iterations of **CELL** explained below, also structures for $y = 0, 1$ are sampled and used to enlarge the training set for the CE.

and a new CE and configurational sampling (red crosses in c) are performed. Again, new ground states (blue squares) are predicted. The corresponding *ab-initio* energies are presented in panel d). With the enlarged training set, the predictions of the ground state energies are quite good for $x \leq 4$. Again, the *ab-initio* energies are added to the training set and a new configurational sampling is performed (red crosses in e). The predicted ground state configurations are indicated with magenta squares. In panel f), the corresponding calculated *ab-initio* energies are represented by magenta dots.

From panels b), d) and f), it can be noted that, while enlarging the *ab-initio* training set leads to improvements of the predictions for low Ni content, the same is not true for $x > 4$, where the predictions are consistently poor. To overcome this problem, the data set was split into a subset with a total number of Ni atoms and vacancies $N_{\text{sub}} = x + y \leq 4$ and a subset with $N_{\text{sub}} > 4$. This procedure was inspired by [22], where the CE as implemented in **CELL** was applied to the $\text{Sr}_8\text{Al}_x\text{Si}_{46-x}$ clathrate. In that work, it was shown that by splitting the training set at the point where strong departures from linearity are observed for E_{mix} vs x , leads to a notable improvement of the predictions of the CE. As can be seen in Fig. 5.1, the *ab-initio* energy of mixing presents a kink above the charge compensated composition $x = 3$ (this kink is also observed at the charge compensated composition for other values of y , not shown in this figure).

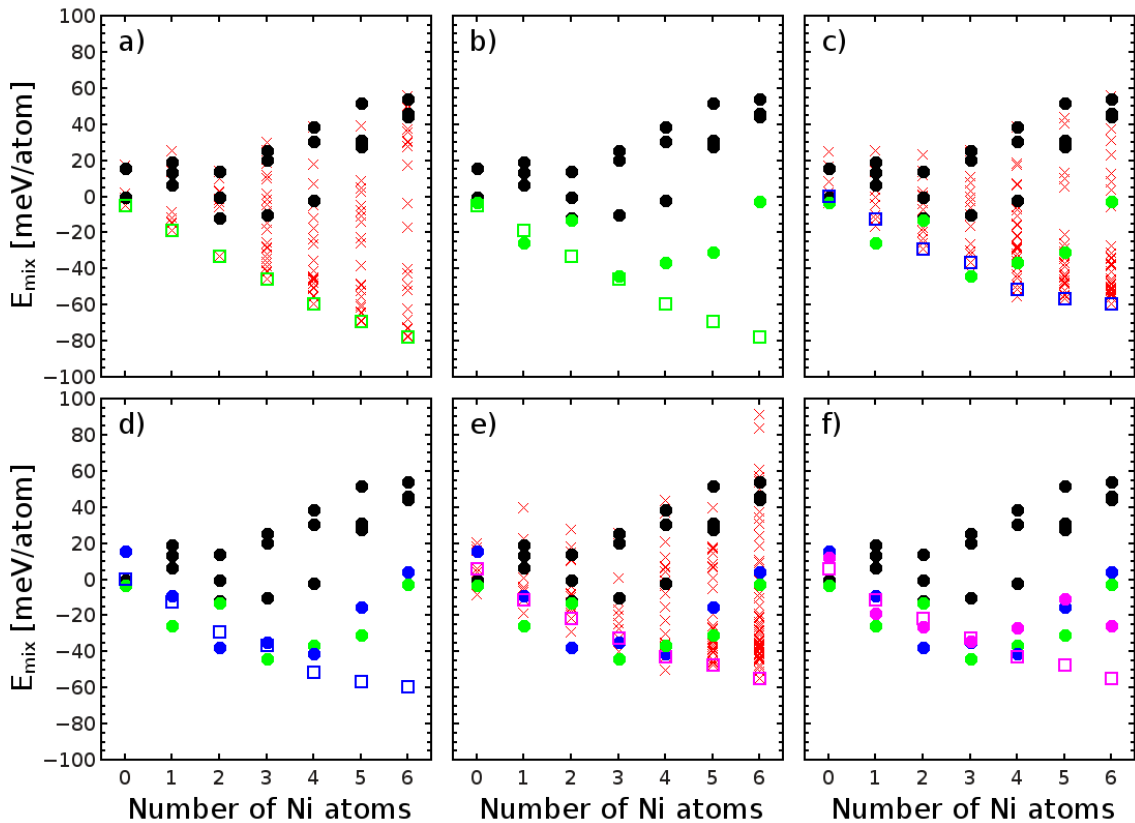


Figure 5.1.: Ground-state search for the unrelaxed set and $y = 2$. Solid circles (\bullet) refer to *ab-initio* calculations, red crosses (\times) represent energies, predicted by Metropolis samplings of the configurational space with the CE, and empty squares (\square) refer to GS predictions in every iteration. Colors are used to distinguish between different iterations of **CELL**: Random structures are represented in black, while structures from the first, second and third iterations are represented in green, blue and magenta, respectively. The panels a) - f) illustrate the progress of the GS search.

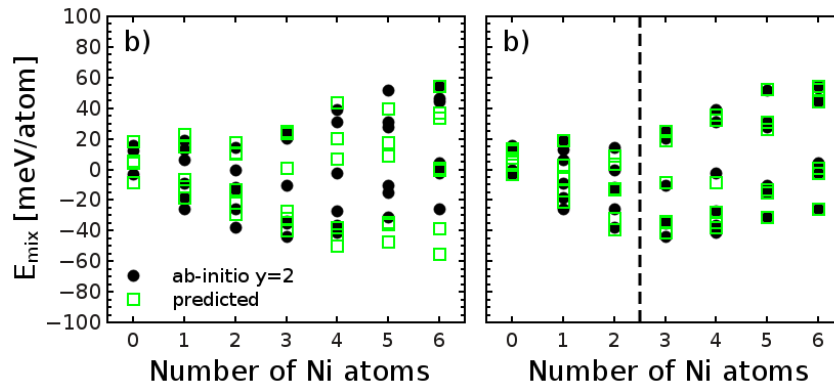


Figure 5.2.: Comparison between non-split (a) and split (b) CE for $y = 2$. The splitting point is indicated with a dashed vertical line.

The benefits of this method are presented in Fig. 5.2. Here, black dots represent *ab-initio* calculations and green squares represent the predicted energies. In panel a), all structures were used to generate a single CE. In panel b) the data set is split (indicated by the dashed line), and two CEs are constructed, one for each data set. For $y = 0$ and $y = 1$ the data is split at $x = 4.5$ and $x = 3.5$, respectively. From comparing panel a) and b) it can be concluded that this splitting procedure greatly improves the quality of the predictions of the CE.

Figure 5.3 presents the investigated composition range. The red dots indicate charge compensated compositions. The dashed line indicates the split of the data sets.

To illustrate the benefits of this approach, the ground-state search with the split CE is shown for $y = 2$ in Fig. 5.4. In this figure, dots refer to *ab-initio* calculations, as in Fig. 5.1. Using the CEs constructed from the split *ab-initio* data, the configuration space is independently sampled in every side of the split point at $x = 2.5$ (red crosses in panel a) and new lowest non-degenerate structures are predicted (purple squares in panel b). In panel c), the *ab-initio* energies of the predicted low energy structures are presented with purple dots.

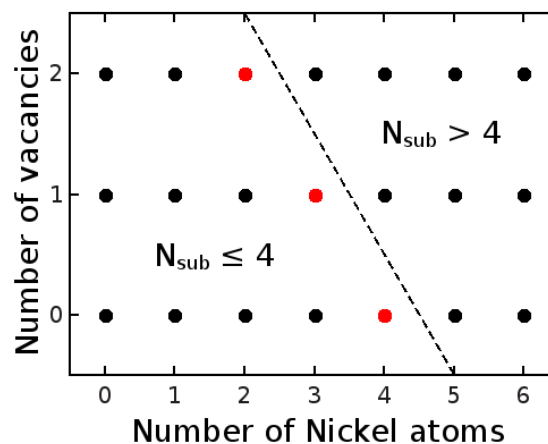


Figure 5.3.: Compositions investigated in this work. Dots represent compositions. The dashed line indicates the splitting of the cluster expansion. Red circles indicate charge balanced compositions.

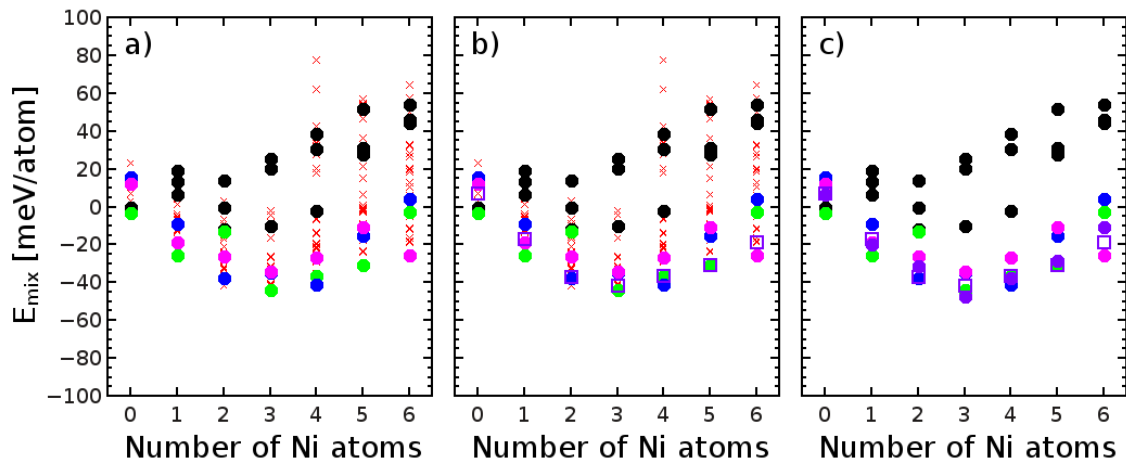


Figure 5.4.: Ground state search for $y = 2$ with the split CE. Circles (\bullet) indicate *ab-initio* calculations, crosses (\times) indicate energies of configurations that are investigated by Metropolis samplings and empty boxes (\square) indicate predictions of low energy structures. The iterations are color coded: green indicates the first, blue the second, magenta the third and purple the fourth iteration. Compared to Fig. 5.1, predictions (b) fit the *ab-initio* calculations (c) much better.

Two conclusions can be made from this figure. First, the split CE increases the predictive power of the cluster expansion. Second, surprisingly, most ground state structures were found before the split was applied. The increase of the predictive power in Fig. 5.4 follows well the findings in reference [22].

5.1.1. CE based on unrelaxed structures

Starting from a set of random structures, the GS search was performed as described above. Once the GS search is complete, the full *ab-initio* data set consists of 164 structures.

Figure 5.5 presents the results of the GS search. In this figure, dots represent *ab-initio* energies and squares represent fittings with the cluster expansion. Red dots and red squares indicate the last iteration of the GS search. Orange crosses indicate the GS structures. Since the energies of the structures from the last iteration have higher energies than the ground states, the last sampling did not introduce any new ground-state structures. For this sampling, more than 10,000 configurations per composition were investigated (i.e. $\sim 10^6$ configurations in the whole composition range). Thus, the configurational space is extensively sampled.

The cross-validation (CV) score of the final cluster expansion is

$$CV_1 = 5.07 \frac{\text{meV}}{\text{atom}}$$

for $N_{\text{sub}} \leq 4$ (90 structures), using 183 clusters, including up to four-point clusters and

$$CV_2 = 7.59 \frac{\text{meV}}{\text{atom}}$$

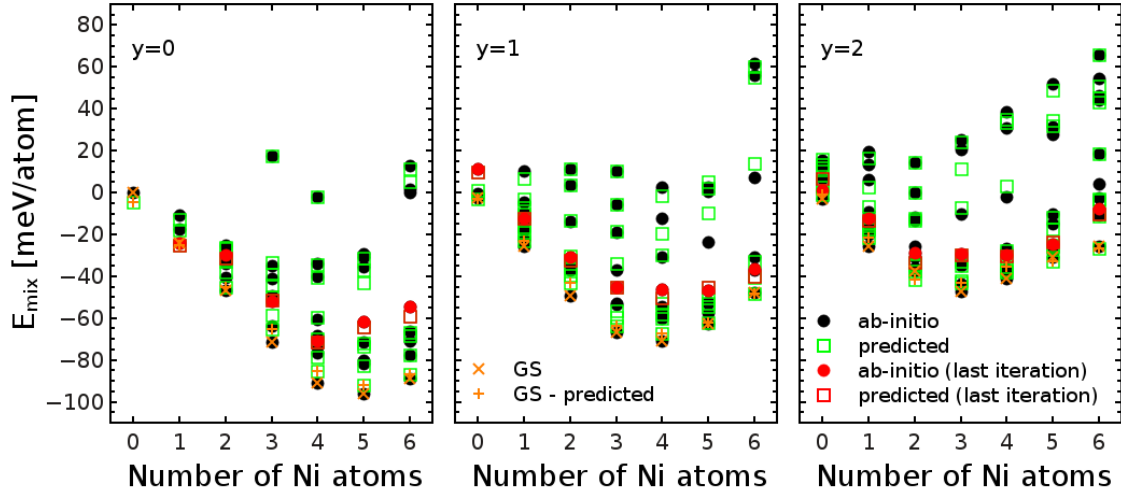


Figure 5.5.: Ground states of the data set of unrelaxed structures. Dots represent *ab-initio* calculations, squares represent fittings with the CE. Red dots and squares indicate the results from the last iteration. *Ab-initio* and predicted energies of ground-state structures are indicated with orange crosses.

for $N_{\text{sub}} > 4$ (74 structures), with 32 clusters, including up to three-point clusters. This accuracy allows us to distinguish between small configurational changes as those between configuration 3 and 4 in Tab. 4.1.

Figure 5.6 presents an overview of the selected clusters from the unrelaxed set.

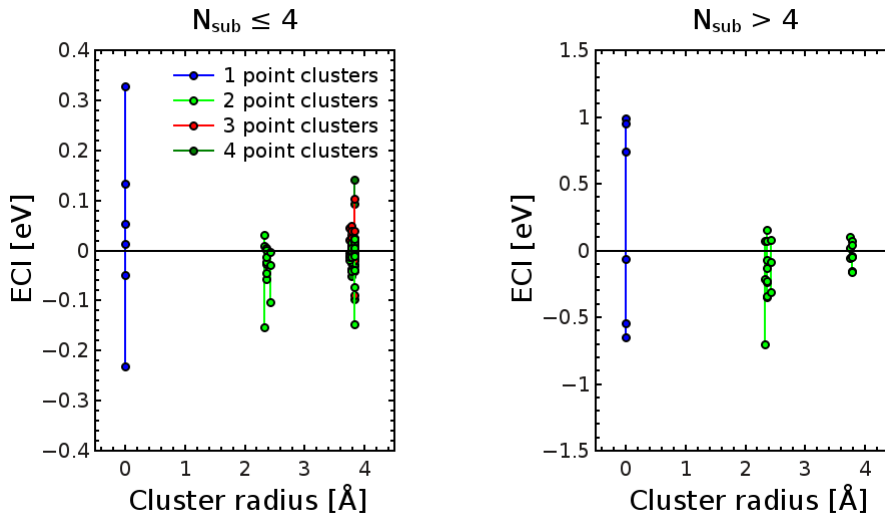


Figure 5.6.: Effective cluster interactions for the unrelaxed structure set. For the set with $N_{\text{sub}} \leq 4$, 183 clusters were selected, including up to four point clusters. For the set with $N_{\text{sub}} > 4$, 32 clusters were selected, including up to two point clusters.

In this figure, the effective cluster interactions (ECI) are presented as a function of the cluster radius. Colors refer to the number of lattice sites for each cluster. The ECIs decrease with the number of sites and cluster radius. This is physically meaningful, because short range interactions are expected to have the largest contribution. This finding justifies the choice of the cluster selection introduced in Sec. 3.3.

5.1.2. CE based on relaxed structures

The construction of the *ab-initio* data set proceeds in a similar way as explained above, starting from random structures and then adding more structures in each iteration of **CELL**. The final relaxed structure set consists of 90 structures, including 53 structures with $N_{\text{sub}} \leq 4$ and 37 structures with $N_{\text{sub}} > 4$. The results are presented in Fig. 5.7 (the symbols have the same meaning as in Fig. 5.5).

The final CVs of the relaxed set are:

$$CV_1 = 14.05 \frac{\text{meV}}{\text{atom}}$$

$$CV_2 = 13.59 \frac{\text{meV}}{\text{atom}}.$$

Fig. 5.8 presents the ECIs of the relaxed data set. For $N_{\text{sub}} \leq 4$, 18 clusters are selected, including up to two point clusters. For $N_{\text{sub}} > 4$, 10 clusters are selected, including up to two point clusters. The number of selected clusters is considerably smaller than for the unrelaxed structure set.

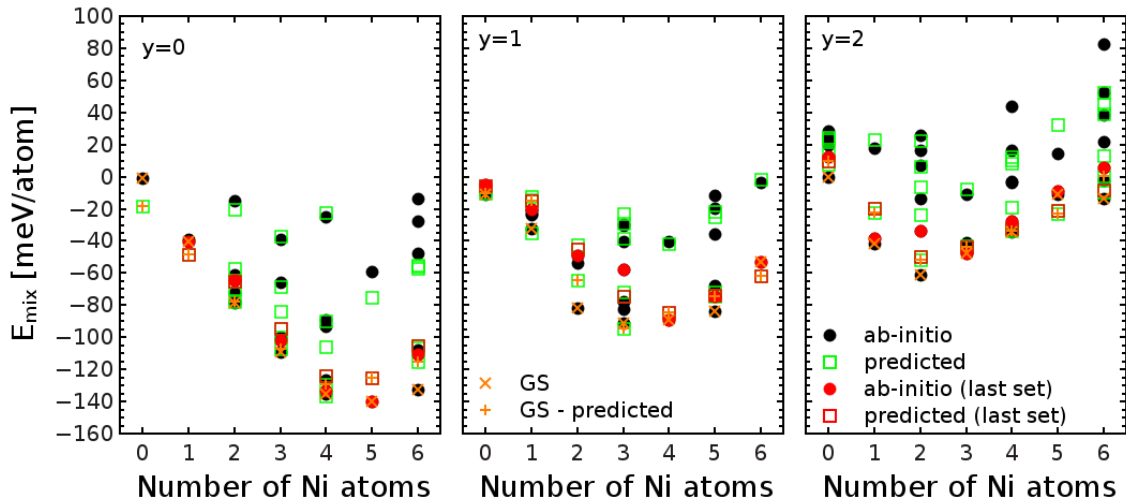


Figure 5.7.: Results of the ground-state search with relaxed structures. Dots represent *ab-initio* calculations, squares represent fittings with the CE. Red dots and squares indicate the results from the last iteration. Orange crosses indicate the GS energies and their predicted values, respectively.

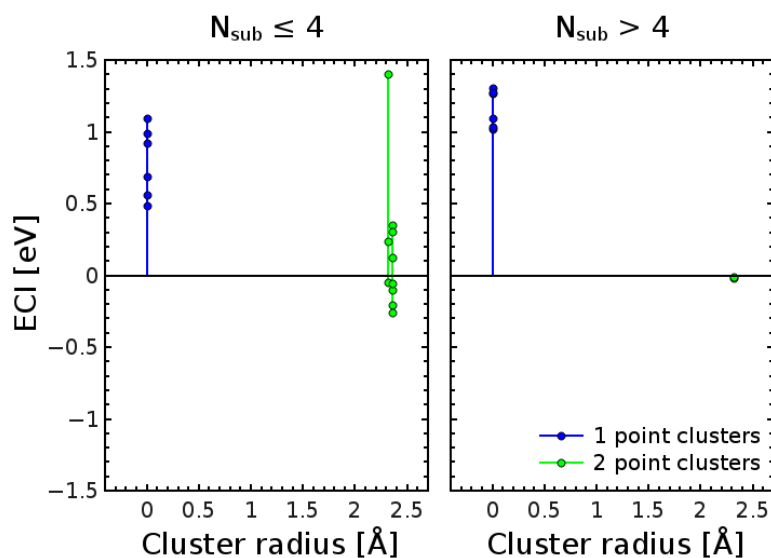


Figure 5.8.: Effective cluster interactions (ECI) for the relaxed structure set. For the set with $N_{\text{sub}} \leq 4$, 18 clusters were selected, including up to two point clusters. For the set with $N_{\text{sub}} > 4$, 10 clusters were selected, including up to two point clusters.

5.1.3. Effect of relaxation

One important aim of this thesis is to find whether the GS search done with non-relaxed structures still yield reasonable GS structures. This is an important issue, since the numerical effort to generate the relaxed set is much higher than for the unrelaxed set. To answer this question, the ground-states of both structure sets are compared². Figure 5.9 shows, for each composition, which GS structures were found by both samplings (blue circles), which ones only by the GS search in the unrelaxed set (red circles) and which ones only by the GS search in the relaxed set (green circles). Most interestingly, it is found that many ($\sim 50\%$) of the GS were found by both approaches, indicating that for a fast screening of the configurational space, the approach employed in the unrelaxed set may be useful.

Nevertheless, since some of the final GS structures have only been selected in the relaxed structure set, structural relaxations should not be omitted for the search of ground-state structures. This suggests the following approach: First the configurational space is screened with unrelaxed structures to approximate the GSs. The low-energy structures, obtained by this screening, are fully relaxed. Then the GS search is completed with additional samplings, using a CE based on the relaxed low-energy structures.

The CVs of the relaxed set are larger than the corresponding CVs for the unrelaxed data set. One possible reason for this poorer performance of the relaxed set may be caused by the fact that the number of structures in the relaxed set contains 74 less structures than the unrelaxed one. Another reason may be the fact that the large distortions in the relaxed set turn the cluster basis representation less adequate. In order to answer this question, 74 structures were removed manually from the unrelaxed set to match the number of structures of the relaxed set. The

²In order to make a meaningful comparison, the GS structures from the unrelaxed set were fully relaxed.

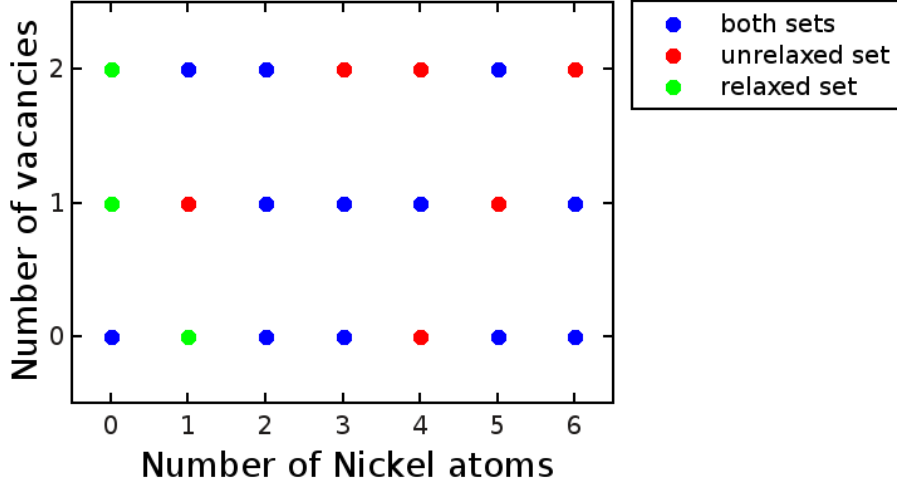


Figure 5.9.: Assignment of final ground-state configurations to the structure set, that they were found with. Blue (red, green) dots indicate compositions, whose GS configurations were found in both (the unrelaxed, the relaxed) sets, respectively.

resulting CVs are: $CV_1 = 6.93$ meV/atom and $CV_2 = 5.68$ meV/atom, i.e. still considerably lower than the CV of the relaxed set. Thus, evidently the reason must be searched in the effect of the relaxation. For relaxed structures, the clusters may not represent the real configurations well, because of the structural changes that are introduced by the relaxation.

5.2. Properties of the ground-state configurations

In this section, the thermodynamical stability, as well as the structural and electronic properties of the ground-state structures are presented.

5.2.1. Thermodynamic stability

One important question concerns the thermodynamical stability of the found GS structures. Here, the stability at zero temperature is addressed by calculating the energy of formation E_{form} for every ground state structure S with total energy E_S :

$$E_{\text{form}}(x, y) = E_S - x \cdot \mu_{\text{Ni}} - y \cdot \mu_{\square} - (46 - x - y) \cdot \mu_{\text{Ge}} - 8\mu_{\text{Ba}} \quad (5.2)$$

$$= E_S - x \cdot (\mu_{\text{Ni}} - \mu_{\text{Ge}}) - y \cdot (\mu_{\square} - \mu_{\text{Ge}}) - 46\mu_{\text{Ge}} - 8\mu_{\text{Ba}} \quad (5.3)$$

$$= E_S - x \cdot \Delta\mu_{\text{NiGe}} - y \cdot \Delta\mu_{\square\text{Ge}} - 46\mu_{\text{Ge}} - 8\mu_{\text{Ba}}, \quad (5.4)$$

where x and y are the number of Ni atoms and vacancies, respectively, and μ_X is the chemical potential of species X . From Eq. (5.4), E_{form} can be calculated for each ground-state structure, for a wide range of chemical potential differences $\Delta\mu_{\text{NiGe}}$ and $\Delta\mu_{\square\text{Ge}}$. For each choice of these potential differences, the most stable structure amongst the ground states is the one with the lowest E_{form} .

The chemical potentials used in Eq. (5.4) can be estimated from the total energies of the bulk materials: $\mu_{\text{Ge}} = -57038.87$ eV, $\mu_{\text{Ni}} = -41316.17$ eV, and $\mu_{\text{Ba}} = -221312.7$ eV. Using these values, the stability is explored in a range of energies around $\Delta\mu_{\text{NiGe}} \approx 15722.7$ eV and $\Delta\mu_{\square\text{Ge}} \approx 57040$ eV. This is shown in Fig. 5.10. Here, each colored area corresponds to a stable structure from the set of ground state structures, whose composition (x, y) is indicated with a label. The horizontal red line indicates a choice of $\Delta\mu_{\square\text{Ge}}$ that leads to experimentally observed stable structures (see Fig. 5.12 below). The vertical red line indicates the $\Delta\mu_{\text{NiGe}}$ estimated above. The usefulness of this result is that the configurations that do not show up in this diagram are not stable for any value of the chemical potentials.

All configurations for which stable structures are thermodynamically allowed, are presented in Fig. 5.11. Here, each dot represents a composition with a stable ground-state structure. The red dot indicates that this structure is charge compensated.

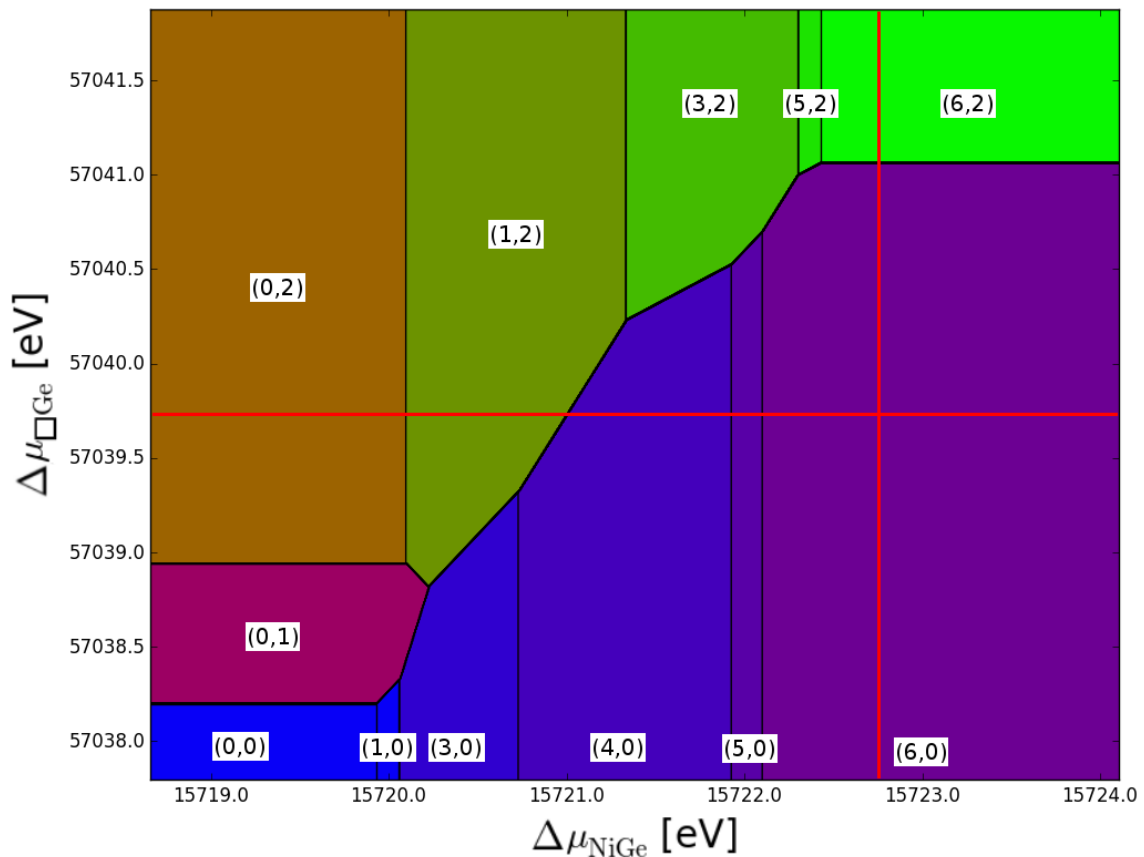


Figure 5.10.: Phase diagram of the $\text{Ba}_8\text{Ni}_x\text{Ge}_{46-x-y}\square_y$ clathrate. Plotted are the compositions with the lowest energy of formation as a function of the difference in chemical potential μ with respect to germanium. The energy of formation is calculated with Eq. 5.4. The horizontal red line indicates a constant a value $\mu_{\square\text{Ge}}$ that leads to stable compositions similar to the experimental results, the vertical red line indicates the value of $\Delta\mu_{\text{NiGe}}$ that has been estimated from the bulk references.

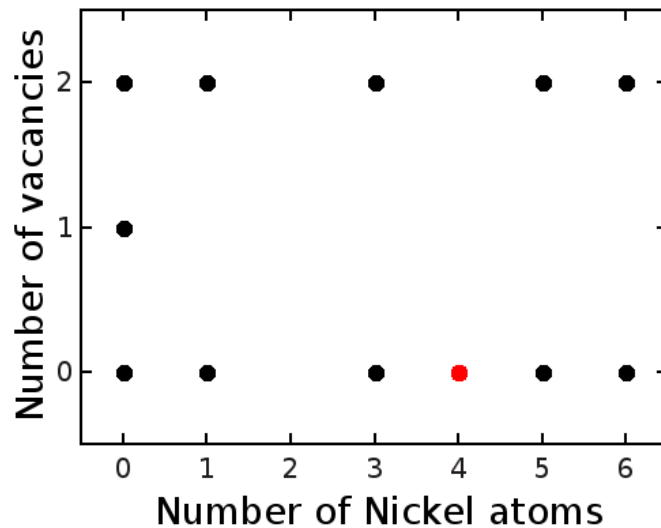


Figure 5.11.: Stable structures, referring to Fig. 5.10. Dots indicate the composition of stable ground state structures. The red dot indicates, that this structure is charge compensated.

5.2.2. Structural properties

The lattice constants of all ground-state structures are presented in Fig. 5.12. Panel a) shows all lattice constants of the relaxed ground state structures (full circles). Solid lines represent the estimate of the lattice constant with Vegard's law. Panel b) presents the lattice constants of the thermodynamically stable structures, together with experimental references.

As seen in Fig. 5.12, the lattice constants decrease as the number of Ni atoms and vacancies increase. The experimental lattice constants are underestimated by $\sim 2\%$. This underestimation is typical for LDA calculations.

Panel b) uncovers two important facts: First, except for only the two compositions

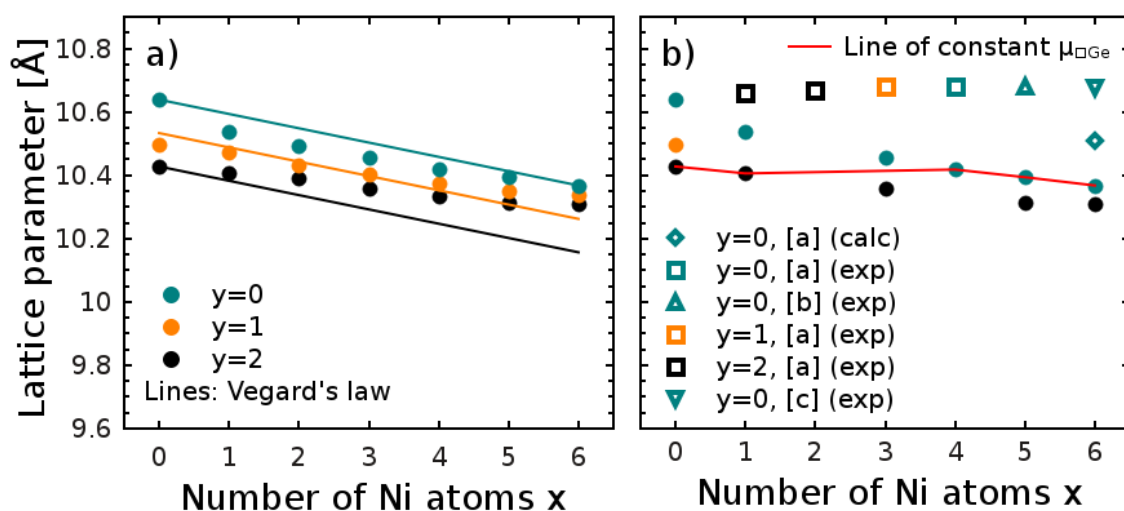


Figure 5.12.: a) Lattice constants of the GS configurations. Solid lines represent the estimate with Vegard's law. b) Stable structures, referring to Fig. 5.10. The red line connects structures that are found for a constant choice of $\Delta\mu_{\square\text{Ge}}$. References: [a] = [3], [b] = [24], [c] = [5]

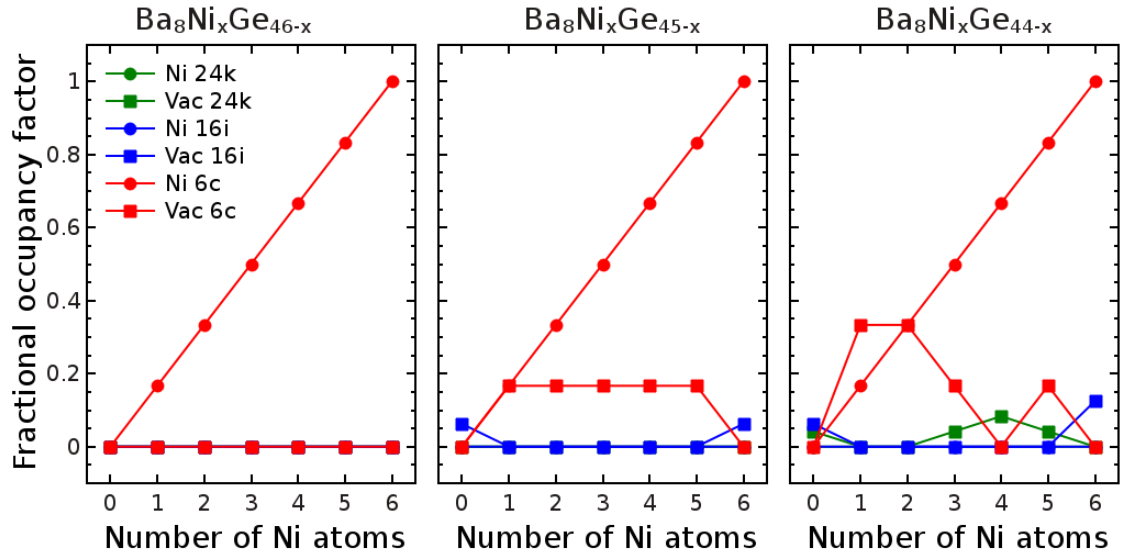


Figure 5.13.: Fractional occupancy Factors of the ground state configurations. Circles represent Ni atoms, squares represent vacancies. 24*k*-sites are indicated in green, 16*i*-sites in blue, and 6*c*-sites in red.

(2, 2) and (3, 1), all stable compositions observed in experiment are also predicted from the phase diagram of Fig. 5.10 by choosing a constant value of $\Delta\mu_{\square\text{Ge}}$ (red line in Fig. 5.10). Second, the lattice constants of these theoretically determined GS structures show a similar trend as the experimental values, i.e., an almost constant value of a (red line in Fig. 5.12).

An important structural property is the so-called fractional occupancy factor (OF). This quantity indicates the degree of occupation of the different Wyckoff sites of the parent lattice by the substitutional species, in this case Ni atoms or vacancies. They are defined precisely by $OF_{Xw} = n_{Xw}/m_w$, with n_{Xw} the number of substitutional species of type X (=Ni, \square) in Wyckoff site w (= 24*k*, 16*i*, or 6*c*), and m_w the multiplicity of Wyckoff site w . For clathrates, the direct experimental determination of the OFs is very difficult, therefore they are usually estimated from the bond distances, which can be directly measured [25]. Unfortunately, for the compositions in this study, there is no experimental data available, neither bond distances, nor OFs. Therefore, the predictions for these quantities presented below could motivate further experimental research in this area.

The OFs of Ni (circles) and vacancies (squares) for the GS structures are presented in Fig. 5.13. From this figure, a distinct preference for the occupation of 6*c*-sites for Ni atoms can be observed. The occupation of the 6*c* site rises with increasing Ni content x until all 6*c* sites are occupied by Ni atoms. This agrees with [5] and [26], where this behavior was predicted. Also, the 6*c* site tends to become vacant. When both Ni atoms and vacancies are present, i.e. for all structures with $x = 6$ and $y > 0$, the 6*c* site is preferentially occupied by Ni atoms.

The averaged bond lengths between nearest-neighbor Wyckoff sites (dots) and nearest neighbor Ge-Ge and Ge-Ni species (squares) are presented in Fig. 5.14. Nearest neighbor Ni-Ni bonds are not present in the ground-state structures. All bond lengths are found to be nearly constant for all compositions (x, y) , except for the the 24*k*-6*c* bonds, which decrease monotonously with Ni content. This behavior can be understood by first noting that Ge-Ni bonds (grey squares) are

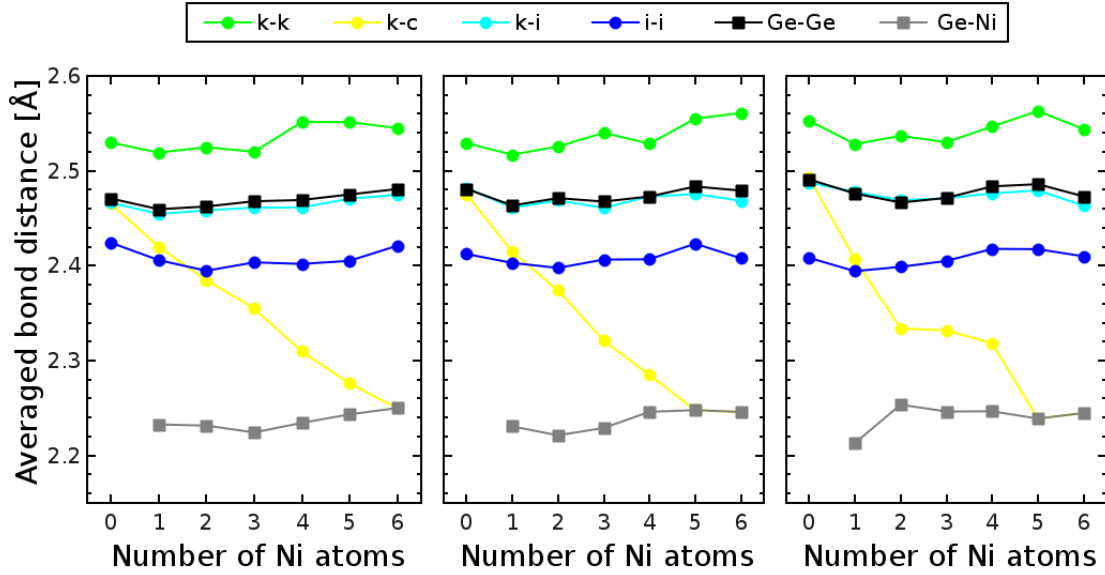


Figure 5.14.: Averaged bond distances for the relaxed ground-state structures of the unrelaxed data set. For all numbers of substituents, k - i bonds are dominated by Ge-Ge bonds. From all types of bonds, bonds between the $24k$ - and the $6c$ -site are the only one decreasing with increasing number of substituents. Lines are guides to the eye.

shorter than Ge-Ge bonds (black squares) by about $\sim 10\%$. Second, since Ni atoms occupy exclusively $6c$ sites (see Fig. 5.13), the bond lengths between k - k , k - i , and i - i (green, cyan, and blue circles, respectively) sites remain mostly unaffected by the addition of Ni atoms. In contrast, the k - c bonds (yellow circles) decrease from a value close to that of Ge-Ge bonds at $x = 0$, to a value close to that of Ge-Ni bonds at $x = 6$.

5.2.3. Electronic structure

Here, the KS eigenvalue spectrum is analyzed for the GS structures of selected compositions. Of particular interest are the charge-balanced compositions $(4,0)$, $(3,1)$, and $(2,2)$. The unbalanced compositions $(4 + \eta, 0)$, $(3 + \eta, 1)$, and $(2 + \eta, 2)$, $\eta = \pm 1$ are also studied. This is motivated by experimental observations that indicate both p - and n -type behavior, as expected for $\eta = +1$ and $\eta = -1$, respectively.

The electronic band structures for the compositions mentioned above are displayed in Fig. 5.15. The central panels correspond to charge-balanced compositions, while left and right panels correspond to unbalanced ones. The displayed region is limited to 2 eV around the Fermi level. An important feature of all the band-structures is that they show a pseudo band-gap³ or a band-gap, that is centered at the Fermi level for charge-balanced compositions and below (above) the Fermi level for $\eta = -1$ ($\eta = +1$). For instance, for $y = 0$ (first row of panels), a band-gap below the Fermi level⁴ is observed for $\eta = -1$, a pseudo band-gap at the Fermi

³i.e. a minimum in the electronic density of states with very few states

⁴Here, the expression "band-gap below (above) the Fermi level" refers to an energy range below (above) the Fermi level, where no electron states exist.

level is observed for the charge-balanced composition $(4, 0)$, and a band-gap above the Fermi level is observed for $\eta = +1$. A similar behavior is obtained for $y = 1$ (second row) and $y = 2$ (third row).

Figure 5.16 presents the electronic density-of-states (DOS) for the ground-state configurations with composition $(4 + \eta, 0)$, $\eta = -1, 0, 1$ (corresponding to the first row of panels in Fig. 5.16). As expected from the band-structures, a main feature is a band-gap at ≈ -0.45 eV for $\eta = -1$, a pseudo band-gap at the Fermi level, and a band-gap at ≈ 0.35 eV for $\eta = +1$. This is indicative of a transition from n - to p -type behavior (dashed arrow in the figure) around the charge-balanced compound.

The obtained band-gaps are smaller than 0.1 eV. Since it is well known that KS band-gaps underestimate the experimentally observed quasiparticle band-gaps, it is expected that the size of the band-gaps for these structures are larger if many-body approaches (such as the GW method) are used for their calculation [19].

In Fig. 5.16, the composition labels (x, y) in red color indicate thermodynamically stable structures, according to the phase diagram of Fig. 5.10. Interestingly, the n -type compositions $(3, 0)$ and $(1, 2)$, as well as the p -type compositions $(5, 0)$ and $(3, 2)$, are stable. This is an important finding, since, as discussed in Chap. 1, obtaining n - and p -type behavior in the same base material is beneficial for the construction of thermoelectric devices.

The obtained results agree well with previously reported calculations in recent publications. More specifically, the pseudo band-gap for $(4, 0)$ agrees with a previous calculation reported in [3]. Also, the DOS for the GS with composition $(6, 0)$ shown in Fig. 5.17 compares well with Fig. 5 in [5].

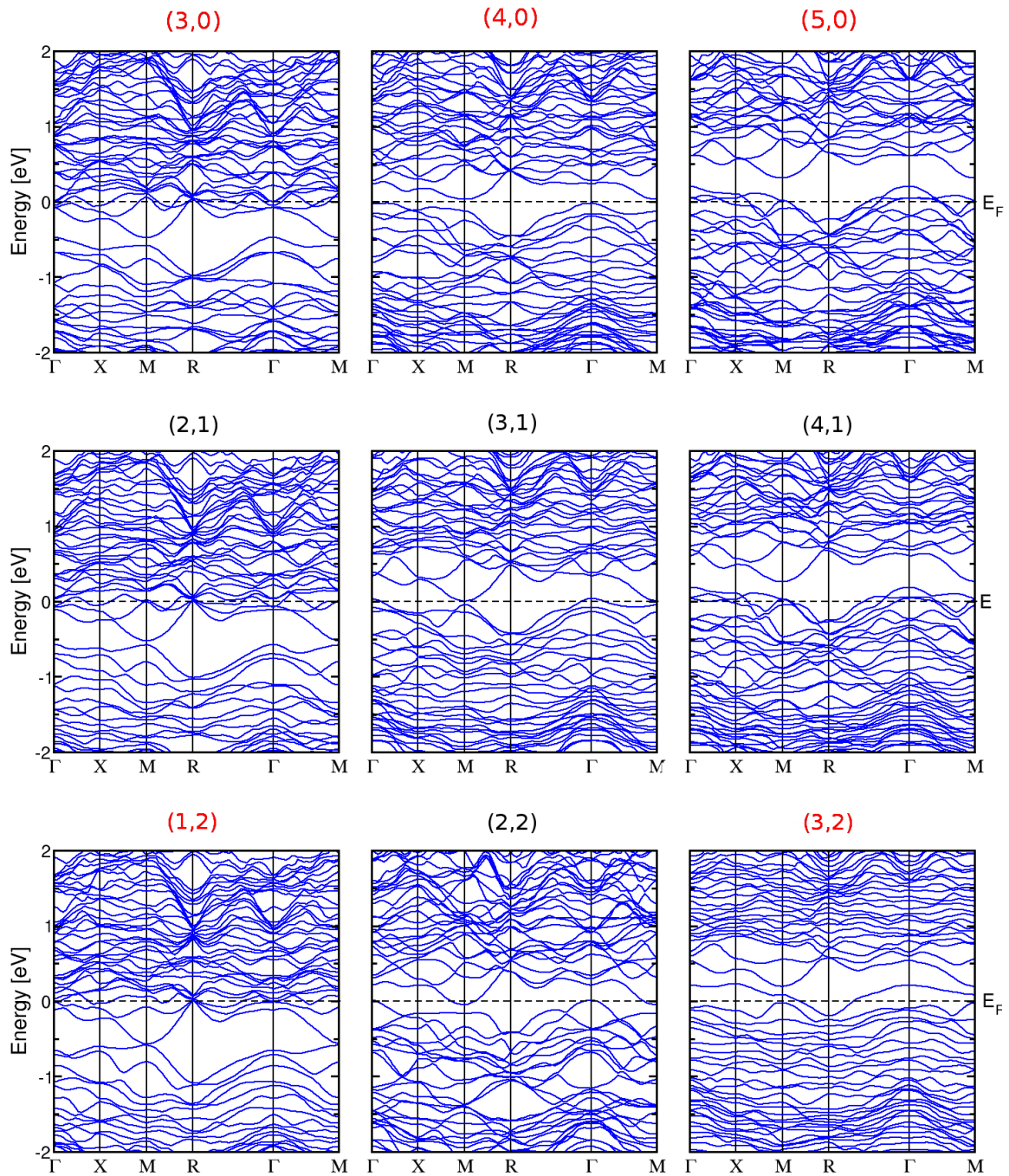


Figure 5.15.: Calculated band structures for $N_{vac} \in (0, 1, 2)$, around the charge-balance point. The Fermi energy is set to 0 and is indicated with a dashed line. For all number of vacancies, a transition from n - to p -type conductivity is present at the charge-balanced composition.

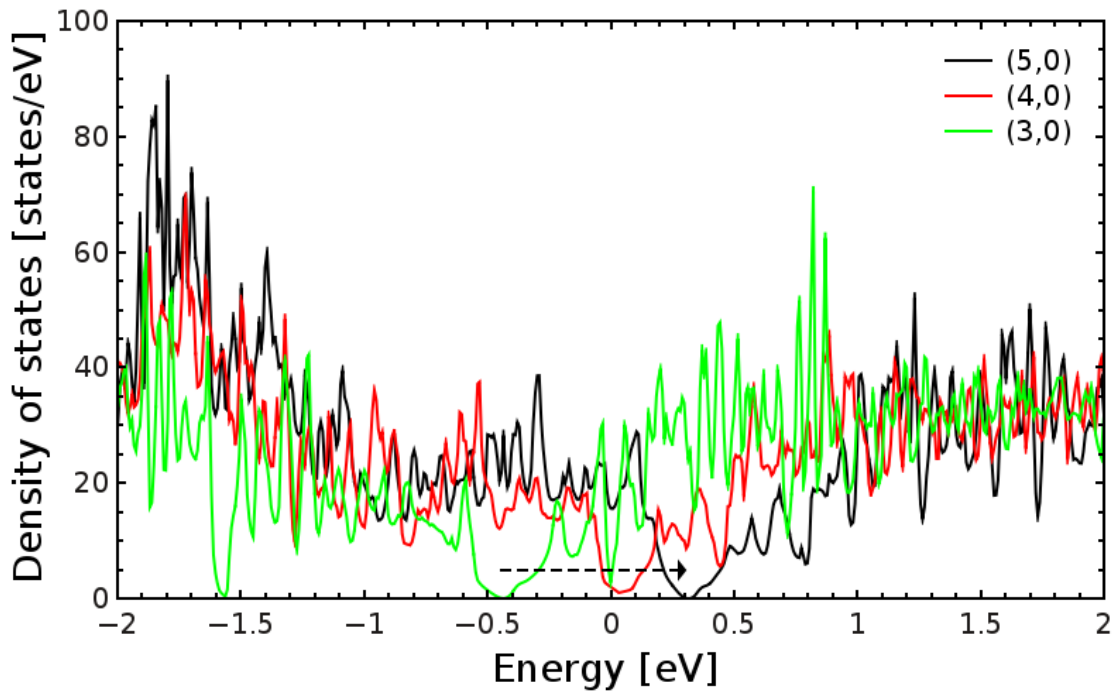


Figure 5.16.: Density of states at the Fermi level for the compositions $x = 3 - 5, y = 0$. All three curves are aligned such that the Fermi level is located at 0 eV. The minimum in the DOS is a band gap below the Fermi level for (3,0), a minimum of the DOS at the Fermi level for (4,0) and a band gap above the Fermi level for (5,0). The dashed arrow indicates this shift of the minimum.

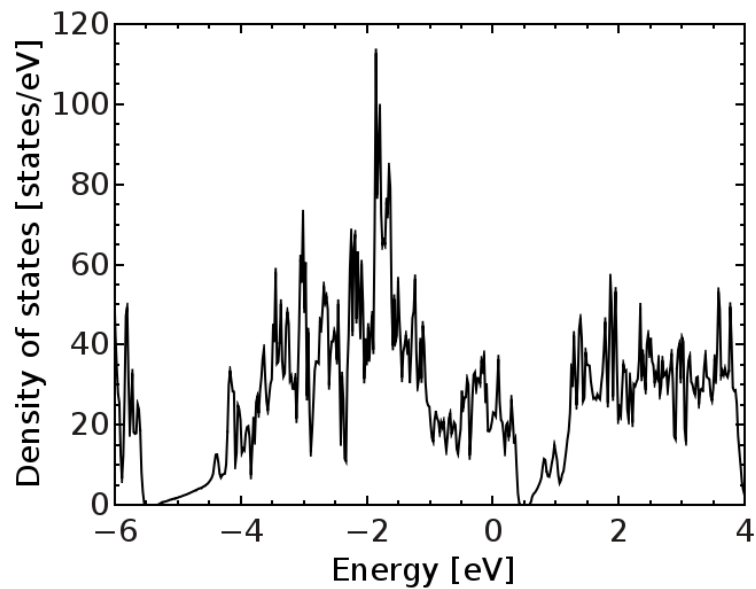


Figure 5.17.: Calculated density of states for composition $(x = 6, y = 0)$. All Ni atoms in this structure are located at 6c-sites.

In this work, a density-functional theory *ab-initio* study of the type-I clathrate compound $\text{Ba}_8\text{Ni}_x\text{Ge}_{46-x-y}\square_y$ ($x \in [0, 6], y \in [0, 2]$) was performed using the DFT package **exciting**. An accurate *ab-initio* description of the structural and electronic properties of $\text{Ba}_8\text{Ni}_x\text{Ge}_{46-x-y}\square_y$ was obtained. To achieve this goal, the cluster expansion technique as implemented in **CELL**, was used to find the ground-state (GS) configurations. In this way, the GSs were found in a fully unbiased way, without any presumption regarding previous knowledge for other clathrate compounds. A good agreement with available experimental data concerning the lattice parameters of the thermodynamically stable structures at different compositions was obtained. For charge-balanced compositions (i.e. those with a closed-shell valence configuration in the host lattice) a pseudo band-gap at the Fermi level is revealed, while for charge-unbalanced compositions either *p*- or *n*-type behavior is found. These findings are fully compatible with reported measurements uncovering semiconducting behavior for charge-balanced compositions and a *n*- to *p*-type transition for unbalanced ones.

It was found that performing CEs based on non-relaxed structures may be useful to obtain a good starting set of structures for a fully relaxed structure set.

The stability of these ground-state configurations was studied. From the stable structures, four have been observed in experiment, whereas two compositions that are observed in experiment are not found to be stable in this work. The stable structures are compatible with an approximately constant value of the chemical potential difference between Ge atoms and vacancies.

The lattice constants of the thermodynamically stable structures underestimate the experimental values from literature by $\sim 2\%$. This underestimation is typical from DFT calculation in the LDA approximation.

The occupation factors of the Wyckoff sites with Ni atoms and vacancies are investigated. It is found, that for all compositions the *6c*-site is preferentially occupied by Ni atoms. Vacancies appear in the ground-state structures on all three distinct Wyckoff sites. When the *6c* site is not fully occupied by Ni atoms, these sites are preferred to become vacant for most of the ground-state structures.

The bond distances between pairs of Wyckoff-sites is studied. It is found, that all of them stay nearly constant for all Ni contents and number of vacancies, except for the bond distance between the *24k* and *6c* site, that is decreasing for increasing Ni content, i.e. for a larger occupation of the *6c*-site with Ni atoms. Thus, it can be concluded, that the decrease in the lattice constant for fixed number of vacancies is driven by the decreasing bond distances between the *24k* and *6c*-site.

Convergence tests are used to determine the required input parameters for *ab-initio* calculations. Parameters are converged, when the examined property (e.g. the total energy) does not significantly change after refining the parameters.

First, the energy differences that are introduced by small configurational changes are tested. Thus, the energy range that is covered by different configurations of atoms for a given concentration is tested.

Both structure and volume optimization are tested to their sensitivity to changes of computational parameters.

The most influencing parameters are 'ngridk', the number of points that are used to discretize the reciprocal space, and 'rgkmax', a parameter that controls the number of basis functions used for solving the Kohn-Sham equations (see chapter 4).

A.1. Convergence of energy differences for different configurations

To test the effect of small configurational changes to the energy, five different configurations with composition $\text{Ba}_8\text{Ni}_3\text{Ge}_{43}$ and different neighboring relations of the substitutional the Ni atoms are chosen. These configurations are presented in section 4.4.

For these configurations, the influence of the energy differences are studied separately for ngridk and rgkmax. All energy differences are shown in reference to configuration 4. The results of the test for ngridk are presented in table A.1. To obtain these values rgkmax was kept constant at $\text{rgkmax} = 6$. In this table, it can be seen, that the energy differences for the different configurations stay nearly constant for all tested k-grid. Thus, the smallest grid ($\text{ngridk} = 2 \times 2 \times 2$), which leads to the lowest computational cost, is chosen. The same kind of test was performed for rgkmax. Here, $\text{ngridk} = 2 \times 2 \times 2$ is used. The results of this test are presented in table A.2. Here can be seen, that the energy differences for stay nearly constant for each choice of rgkmax. Thus, the smallest value, $\text{rgkmax} = 6$, is chosen.

A.2. Convergence of volume relaxations

To test the effect of the computational parameters on the volume relaxation, volume relaxations for the same configuration were performed for different values of rgkmax and ngridk, and the resulting lattice constants are compared. The results

Configuration ngridk	1	2	3	4	5
$2 \times 2 \times 2$	39.04	9.50	15.14	0	2.23
$4 \times 4 \times 4$	38.99	9.80	15.51	0	2.64
$6 \times 6 \times 6$	39.07	9.83	15.55	0	2.76

Table A.1.: Results of the energy scale test with ngridk. Shown are the total energy differences in meV/atom in reference to configuration 4.

Configuration rgkmax	1	2	3	4	5
6	39.04	9.50	15.14	0	2.22
7	38.45	9.10	14.73	0	2.13
8	38.51	9.06	14.73	0	X

Table A.2.: Results of the energy scale test with rgkmax. Shown are the total energy differences in meV/atom in reference to configuration 4. The X for configuration 5 and rgkmax = 8 denotes, that this ground-state calculation for this set of parameters did not converge.

ngridk rgkmax	$2 \times 2 \times 2$	$4 \times 4 \times 4$	$6 \times 6 \times 6$
6	10.05	10.05	10.05
6.5	10.19	10.19	10.19
7	10.30	10.31	10.31
8	10.45	10.46	10.45

Table A.3.: Results of the lattice constant relaxation test. Table values are lattice constants in Angström. The relaxed lattice constant is not sensitive to ngridk, but changes with rgkmax.

of this test are presented in table A.3. For all values of ngridk, the lattice constant keeps nearly constant. Thus, the smallest value, ngridk = $2 \times 2 \times 2$ is chosen. But the lattice constant varies considerably for different choices of rgkmax. When this parameter is increased, the relaxed lattice constant increases as well. Figure A.1 presents the dependence of the lattice constant on rgkmax for ngridk = $2 \times 2 \times 2$. Here, every dot represents a relaxed lattice constant for a specific choice of rgkmax. The slope of the curve does not suggest a converged behavior for the highest tested value rgkmax = 8. For sampling the configurational space, e.g. for the application of the iterative cluster expansion method with CELL, this is not compellingly necessary. In order to find the ground state configuration, the only requirement is that the energy differences for two different configurations are converged and thus

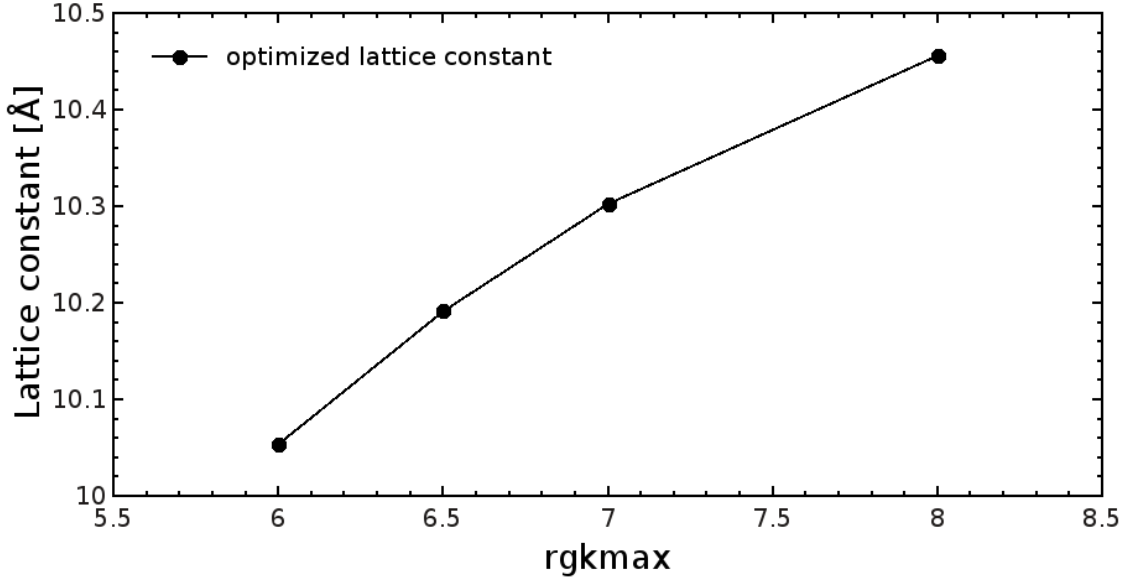


Figure A.1.: Results of the lattice relaxation convergence test. The lattice constant at $\text{rgkmax} = 8$ is not converged. The used \mathbf{k} -grid is " $2 \times 2 \times 2$ ". Values from table A.3.

the order of the configurations is not changed, i.e. a structure that is lower in energy for $\text{rgkmax} = 6$ is still lower in energy for a higher value of rgkmax . To verify this behavior, two configurations are chosen. For both of them, lattice optimizations with $\text{rgkmax} = 6$ and $\text{rgkmax} = 7$ are performed. The results of these calculations are fitted with the Birch-Murnaghan equation of states. Figure A.2 presents the results of this fitting. Here, each curve is a fit with the BM equation of states and corresponds to a configuration with a specific choice of rgkmax . Dots and squares indicate *ab-initio* calculations. For reasons of presentation, all *ab-initio* energies are presented as a difference to the lowest energy value of this set. The distance

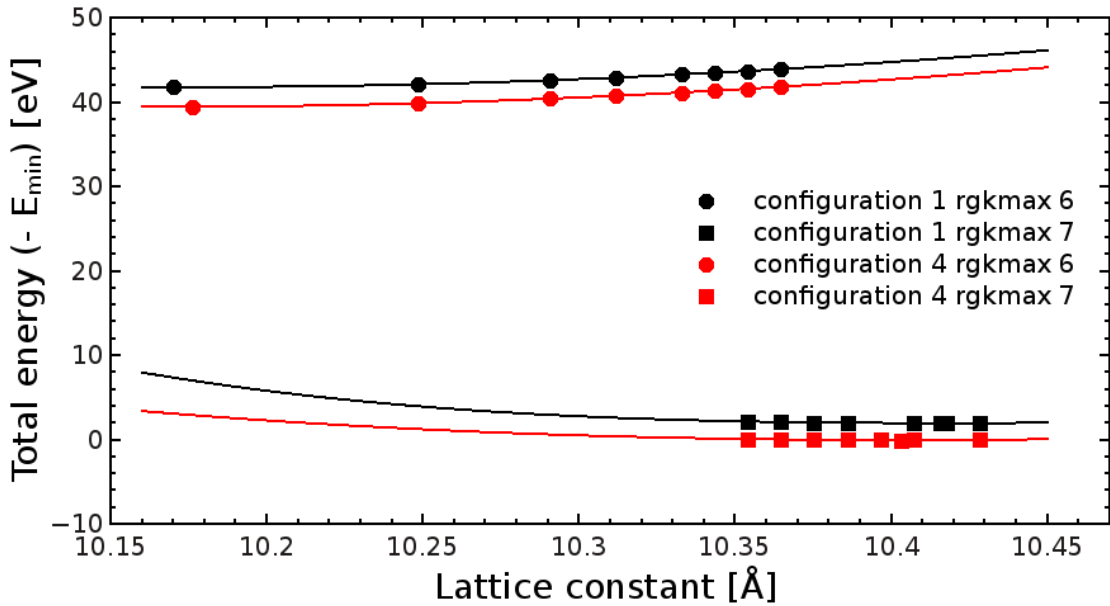


Figure A.2.: Shift of lattice constant relaxation curves with the change of rgkmax . Configurations are described in ???. Solid lines are fitted with the Birch-Murnaghan equation of states (equation 4.11).

between both configurations for $\text{rgkmax} = 6$, i.e. black and red dots in figure A.2,

is similar to the distance of both configurations for $\text{rgkmax}=7$, i.e. the black and red squares in figure A.2. Thus, the difference in energy between configurations stays constant for different lattice constants. Furthermore, if we consider the lattice constant from the calculation with $\text{rgkmax} = 6$ in the environment of $\text{rgkmax} = 7$, i.e. evaluate the energies for $\text{rgkmax}=7$ at the lattice constant, that gives the lowest energies for $\text{rgkmax}=6$, the energy differences would stay constant. Since the curvature of the fittings remains similar for both configurations and parameters, there are no crossings of the functions, so that a configuration lower in energy will stay lower in energy, regardless of the choice of rgkmax .

Due to the results of these tests, $\text{ngridk} = 2 \times 2 \times 2$ and $\text{rgkmax} = 6$ are chosen as parameters for the lattice constant relaxation.

A.3. Convergence of atom relaxation

To test the effect of changing ngridk and rgkmax on atom relaxations, the atomic positions for one structure are optimized for $\text{ngridk} = 2 \times 2 \times 2$ and $\text{rgkmax} = 6$. Afterwards, the parameters are refined and a single self-consistent field iteration is performed. From this, the atomic forces are calculated. If the remaining forces are still below the threshold $\epsilon_{force} = 257.11 \text{ meV}/\text{\AA}$ that was used for the initial structure optimization, the parameters for the relaxation run are converged.

Table A.4 shows the results of this test. Here it can be seen that the remaining forces for using finer parameters are still below this threshold. For this reason, the parameters $\text{ngridk} = 2 \times 2 \times 2$ and $\text{rgkmax} = 6$ are converged and are used for all atom relaxations.

$\frac{\text{ngridk}}{\text{rgkmax}}$	$2 \times 2 \times 2$	$4 \times 4 \times 4$	$6 \times 6 \times 6$
6	213.16	225.28	239.64
7	233.39	X	X
8	237.83	X	X

Table A.4.: Atom relaxation convergence test results. Table values are the maximum module of the forces in $\text{meV}/\text{\AA}$. The entries denoted with a X are not calculated.

- [1] Mercuri G. Kanatzidis. Advances in thermoelectrics: From single phases to hierarchical nanostructures and back. *MRS BELLETIN*, 40:687 – 694, 2015. 1, 1
- [2] G. S. Nolas, J. L. Cohn, G. A. Slack, and S. B. Schujman. Semiconducting ge clathrates: Promising candidates for thermoelectric applications. *Applied Physics Letters*, 73 Nr. 2:178, 1998. 1, 2
- [3] *et.al.* U. Aydemir. Electronic band structure and low-temperature transport properties of the type-i clathrate $\text{Ba}_8\text{Ni}_x\text{Ge}_{46-x-y}\square_y$. *Dalton Transactions*, 44: 7524, 2015. 1, 2.1, 2.2, 5.12, 5.2.3, A.3
- [4] U. Aydemir, C. Candolfi, A. Ormeci, M. Baitinger, N. Oeschler, F. Steglich, and Yu Grin. High temperature thermoelectric properties of the type-i clathrate $\text{Ba}_8\text{Ni}_x\text{Ge}_{46-x-y}\square_y$. *J. Phys.: Condens. Matter*, 26:485801, 2014. 1
- [5] Simon Johnsen, Anders Bentien, Georg K. H. Madsen, Mats Nygren, and Bo B. Iversen. Crystal structure and transport properties of nickel containing germanium clathrates. *Phys. Rev. B*, 76:245126, Dec 2007. 1, 2.2, 5.12, 5.2.2, 5.2.3, A.3
- [6] Anders Bentien, Simon Johnsen, and Bo Brummersted Iversen. Strong phonon charge carrier coupling in thermoelectric clathrates. *Phys. Rev. B*, 73:094301, Mar 2006. 1, 2.2
- [7] Hui Zhang, Jing-Tai Zhao, Mei-Bo Tang, Zhen-Yong Man, Hao-Hong Chen, and Xin-Xin Yang. Structure and low-temperature properties of $\text{Ba}_8\text{Ni}_6\text{Ge}_{40}$. *Journal of Physics and Chemistry of Solids*, 70(2):312 – 315, 2009. ISSN 0022-3697. 1, 2.2
- [8] H. Davy. *Philos. Trans. R. Soc.*, 101:155–162, 1811. 2
- [9] L. Pauling. *J. Am. Chem. Soc.*, 57:2680–2684, 1935. 2
- [10] Mogens Christensen, Simon Johnsen, and Bo Brummerstedt Iversen. Thermoelectric clathrates of type i. *Dalton Transactions*, 39:978–992, 2010. 2.1
- [11] H. Euchner and *et al.* Phononic filter effect of rattling phonons in the thermoelectric clathrate $\text{Ba}_8\text{Ge}_{40+x}\text{Ni}_{6-x}$. *Physical Review B*, 86:224303, 2012. 2.1
- [12] M. Dayah. Retrieved january 10, 2017,. *Dynamic Periodic Table. from Ptable: <http://www.ptable.com>*, 1997, October 1. 2.3, A.3
- [13] J.M. Sanchez, F. Ducastelle, and D. Gratias. Generalized cluster description of multicomponent systems. *Physica*, 128A:334–350, 1984. 3.1, 3.1, 3.1

- [14] A. van de Walle. Multicomponent multisublattice alloys, nonconfigurational entropy and other additions to the alloy theoretic automated toolkit. *Calphad*, 33:266–278, 2009. 3.1, 3.1
- [15] J. M. Sanchez. Cluster expansion and the configurational theory of alloys. *Physical Review B*, 81:224202, 2010. 3.1, 3.2
- [16] A. Hübner. Bachelor thesis, 2016. 3.3
- [17] Lance J. Nelson, Gus L. W. Hart, Fei Zhou, and Vidvuds Ozoliņš. Compressive sensing as a paradigm for building physics models. *Phys. Rev. B*, 87:035125, Jan 2013. 3.3
- [18] S. Rigamonti and *et.al.* Cell. in preparation. 3.4, 3.3, A.3
- [19] A. Gulans, S. Kontur, C. Meisenbichler, D. Nabok, P. Pavone, S. Rigamonti, S. Sagmeister, U. Werner, and C. Draxl. *exciting - a full-potential all-electron package implementing density-functional theory and many-body perturbation theory*. *J. Phys.: Condens. Matter*, 26:363202, 2014. 4, 4.2, 4.2, 5.2.3
- [20] P. Hohenberg and W. Kohn. Inhomogeneous electron gas. *Physical Review*, 136(3B):B 864 – B 871, 1964. 4.1
- [21] W.Kohn and L.J.Sham. Self-consistent equations including exchange and correlation effects. *Phys. Rev.*, 140:A1133, 1965. 4.1
- [22] Maria Troppenz. Structural stability and electronic properties of the thermoelectric clathrates $Ba_8Al_xSi_{46-x}$ and $Sr_8Al_xSi_{46-x}$. Master’s thesis, Humboldt-Universität zu Berlin, 2015. 4.1, 4.3, 5.1, 5.1
- [23] Francis Birch. Finite elastic strain of cubic crystals. *Physical Review*, 71, Nr 11: 809, 1947. 4.3
- [24] Jingtao Xu, Jiazhen Wu, Yoichi Tanabe, Satoshi Heguri, Gang Mu, Hidekazu Shimotani, and Katsumi Tanigaki. Low-temperature physical and thermoelectric properties of $Ba_8Ni_5Ge_{41}$. *Journal of Electronic Materials*, 42(7):2025–2029, 2013. 5.12, A.3
- [25] John H. Roudebush, Clarina de la Cruz, Bryan C. Chakoumakos, and Susan M. Kauzlarich. *Inorganic Chemistry*, 51(3):1805–1812, 2012. PMID: 22191511. 5.2.2
- [26] Gerhard Cordier and Petra Woll. Neue ternäre intermetallische verbindungen mit clathratstruktur: $Ba_8(t,si)_6si_{40}$ und $Ba_6(t,ge)_6ge_{40}$ mit $t \equiv ni, pd, pt, cu, ag, au$. *Journal of the Less Common Metals*, 169(2):291 – 302, 1991. 5.2.2

List of Figures

1.1	Diffusion of charge carriers in a solid due to the presence of a temperature gradient.	1
1.2	Scheme of a thermoelectric generator. Charge carriers (electrons (-) and holes (+)) diffuse from the heat source to the heat sink (see Fig. 1.1), resulting in a voltage V	2
2.1	Type-I clathrate structure. Wyckoff positions are indicated.	4
2.2	Estimate of the number of configurations for a ternary compound with 46 atoms and a maximum of 24 symmetrically equivalent positions.	5
2.3	Electronic configuration of Ge (a) and Ni (b) atoms in the host structure. Nickel atoms need four electrons (red arrows) to acquire the same valence configuration as Ge. Source: [12]	6
3.1	Basis functions as defined in Eq. (3.6). These functions are defined in a discrete space, lines in the plot are guides to the eye.	8
3.2	Root mean square error (RMSE) and cross validation score (CV) as a function of the number of selected clusters.	11
3.3	Workflow of CELL . The steps are described in detail in the text. Figure from [18].	12
4.1	Example of the NM+BM lattice relaxation. All energies are given as a difference to the first calculation of this set. Black dots represent <i>ab-initio</i> energies. The red dot indicates the lattice constant from the BM fit to the black dots. The red curve shows the final fit with the BM equation of states including the red dot. The index of the calculation is indicated by a number.	19
4.2	Convergence of SCL iterations in energy differences $ \Delta E $ to run 1.	19
5.1	Ground-state search for the unrelaxed set and $\gamma = 2$. Solid circles (●) refer to <i>ab-initio</i> calculations, red crosses (×) represent energies, predicted by Metropolis samplings of the configurational space with the CE, and empty squares (□) refer to GS predictions in every iteration. Colors are used to distinguish between different iterations of CELL : Random structures are represented in black, while structures from the first, second and third iterations are represented in green, blue and magenta, respectively. The panels a) - f) illustrate the progress of the GS search.	23
5.2	Comparison between non-split (a) and split (b) CE for $\gamma = 2$. The splitting point is indicated with a dashed vertical line.	24

5.3	Compositions investigated in this work. Dots represent compositions. The dashed line indicates the splitting of the cluster expansion. Red circles indicate charge balanced compositions.	24
5.4	Ground state search for $y = 2$ with the split CE. Circles (●) indicate <i>ab-initio</i> calculations, crosses (×) indicate energies of configurations that are investigated by Metropolis samplings and empty boxes (□) indicate predictions of low energy structures. The iterations are color coded: green indicates the first, blue the second, magenta the third and purple the fourth iteration. Compared to Fig. 5.1, predictions (b) fit the <i>ab-initio</i> calculations (c) much better.	25
5.5	Ground states of the data set of unrelaxed structures. Dots represent <i>ab-initio</i> calculations, squares represent fittings with the CE. Red dots and squares indicate the results from the last iteration. <i>Ab-initio</i> and predicted energies of ground-state structures are indicated with orange crosses.	26
5.6	Effective cluster interactions for the unrelaxed structure set. For the set with $N_{\text{sub}} \leq 4$, 183 clusters where selected, including up to four point clusters. For the set with $N_{\text{sub}} > 4$, 32 clusters where selected, including up to two point clusters.	26
5.7	Results of the ground-state search with relaxed structures. Dots represent <i>ab-initio</i> calculations, squares represent fittings with the CE. Red dots and squares indicate the results from the last iteration. Orange crosses indicate the GS energies and their predicted values, respectively.	27
5.8	Effective cluster interactions (ECI) for the relaxed structure set. For the set with $N_{\text{sub}} \leq 4$, 18 clusters where selected, including up to two point clusters. For the set with $N_{\text{sub}} > 4$, 10 clusters where selected, including up to two point clusters.	28
5.9	Assignment of final ground-state configurations to the structure set, that they were found with. Blue (red, green) dots indicate compositions, whose GS configurations were found in both (the unrelaxed, the relaxed) sets, respectively.	29
5.10	Phase diagram of the $\text{Ba}_8\text{Ni}_x\text{Ge}_{46-x-y}\square_y$ clathrate. Plotted are the compositions with the lowest energy of formation as a function of the difference in chemical potential μ with respect to germanium. The energy of formation is calculated with Eq. 5.4. The horizontal red line indicates a constant a value $\mu_{\square\text{Ge}}$ that leads to stable compositions limilar to the experimental results, the vertical red line indicates the value of $\Delta\mu_{\text{NiGe}}$ that has been estimated from the bulk references.	30
5.11	Stable structures, referring to Fig. 5.10. Dots indicate the composition of stable ground state structures. The red dot indicates, that this structure is charge compensated.	31
5.12	a) Lattice constants of the GS configurations. Solid lines represent the estimate with Vegard's law. b) Stable structures, referring to Fig. 5.10. The red line connects structures that are found for a constant choice of $\Delta\mu_{\square\text{Ge}}$. References: [a] = [3], [b] = [24], [c] = [5]	31

5.13	Fractional occupancy Factors of the ground state configurations. Circles represent Ni atoms, squares represent vacancies. 24 <i>k</i> -sites are indicated in green, 16 <i>i</i> -sites in blue, and 6 <i>c</i> -sites in red.	32
5.14	Averaged bond distances for the relaxed ground-state structures of the unrelaxed data set. For all numbers of substituents, <i>k</i> -i bonds are dominated by Ge-Ge bonds. From all types of bonds, bonds between the 24 <i>k</i> - and the 6 <i>c</i> -site are the only one decreasing with increasing number of substituents. Lines are guides to the eye. . .	33
5.15	Calculated band structures for $N_{vac} \in (0, 1, 2)$, around the charge-balance point. The Fermi energy is set to 0 and is indicated with a dashed line. For all number of vacancies, a transition from <i>n</i> - to <i>p</i> -type conductivity is present at the charge-balanced composition.	35
5.16	Density of states at the Fermi level for the compositions $x = 3 - 5$, $y = 0$. All three curves are aligned such that the Fermi level is located at 0 eV. The minimum in the DOS is a band gap below the Fermi level for (3, 0), a minimum of the DOS at the Fermi level for (4, 0) and a band gap above the Fermi level for (5, 0). The dashed arrow indicates this shift of the minimum.	36
5.17	Calculated density of states for composition ($x = 6, y = 0$). All Ni atoms in this structure are located at 6 <i>c</i> -sites.	36
A.1	Results of the lattice relaxation convergence test. The lattice constant at <code>rgkmax = 8</code> is not converged. The used k -grid is "2 × 2 × 2". Values from table A.3.	III
A.2	Shift of lattice constant relaxation curves with the change of <code>rgkmax</code> . Configurations are described in ???. Solid lines are fitted with the Birch-Murnaghan equation of states (equation 4.11).	III

List of Tables

4.1	Comparison of energies differences $\Delta E_{i,4} = E_i - E_4$ of different configurations of the Ba ₈ Ni ₃ Ge ₄₃ clathrate. The tuples indicate the neighboring relations of the Ni atoms: (No. of nearest neighbors, No. of second nearest neighbors, No. of third nearest neighbors). . .	20
4.2	Computational parameters leading to converged quantities.	21
A.1	Results of the energy scale test with <code>ngridk</code> . Shown are the total energy differences in meV/atom in reference to configuration 4. . .	II
A.2	Results of the energy scale test with <code>rgkmax</code> . Shown are the total energy differences in meV/atom in reference to configuration 4. The X for configuration 5 and <code>rgkmax = 8</code> denotes, that this ground-state calculation for this set of parameters did not converge.	II
A.3	Results of the lattice constant relaxation test. Table values are lattice constants in Angström. The relaxed lattice constant is not sensitive to <code>ngridk</code> , but changes with <code>rgkmax</code>	II

A.4 Atom relaxation convergence test results. Table values are the maximum module of the forces in meV/Å. The entries denoted with a X are not calculated. IV

I'd like to thank Prof. Claudia Draxl for her outstanding supervision, support and encouragement, that allowed me to work on such an interesting topic.

Also, I'd like to thank my mentor Dr. Santiago Rigamonti for his constant support, that not only helped me finishing this work, but also develop my own scientific skills.

Furthermore I thank Maria Troppenz for her valuable advice and interesting discussions.

Thanks to all the members of the SOL-group, that were always friendly and supportive.

Spacial thanks goes to my family and friends, for all the support that was necessary to finish my studies.

Finally, I thank my girlfriend Maria Priebe, who always supports me in whatever I do and helps me to achieve my goals.

I thank the Norddeutscher Verbund für Hoch- und Höchstleistungsrechnen (HLRN) for providing computational resources.

Selbständigkeitserklärung

Hiermit versichere ich, dass ich die vorliegende Arbeit selbständig verfasst und keine anderen als die hier angegebenen Quellen und Hilfsmittel verwendet habe.

Ort, Datum, Unterschrift